Supporting Information for

# Long-Term Solar Energy Storage under Ambient Conditions in a MOF-Based Solid-Solid Phase Change Material

Kieran Griffiths, Nathan R. Halcovitch, John M. Griffin

## DFT Calculation Details

First-principles calculations of NMR parameters were carried out under periodic boundary conditons using the CASTEP code[1] employing the gauge-including projector augmented wave (GIPAW) algorithm,[2] which allows the reconstruction of the all-electron wave function in the presence of a magnetic field. The CASTEP calculations employed the generalised gradient approximation Perdew–Burke–Ernzerhof exchange-correlation functional,[3] and core–valence interactions were described by ultrasoft pseudopotentials.[4]

Prior to calculation of the NMR parameters, structures were fully geometry optimised using the G06 semiempirical dispersion correction scheme[5] and allowing all atomic positions to vary. For calculations on guest-free frameworks, the input atomic co-ordinates were taken from structures published by Dybtsev *et al*., with the guest molecule atoms deleted where appropriate.[6] The tetragonal *lp* structure was based on the empty framework structure, the orthorhombic *np* structure was based on the benzene-loaded structure, and the distorted tetragonal np structure was based on the DMF-loaded structure. These structures also required deletion of some of the atoms representing the dynamic disorder of the DABCO group in order to make a chemically sensible input structure. The structures were then optimized while keeping the unit cell parameters fixed to the experimental values.

Single-molecule calculations were carried out in a 20 × 20 × 20 Å cell with fixed cell parameters to ensure molecules remained isolated from periodic replicas.

Geometry optimisations and NMR calculations were carried out using a planewave energy cut-off of 60 Ry, and for crystal structures, a k-point spacing of 0.05 $2\pi$ $Å^{-1}$ was used. For single-molecule calculations, a single k-point at the fractional coordinate (0.25, 0.25, 0.25) was used. The calculations generate the absolute shielding tensor ($\sigma$) in the crystal frame.

Diagonalisation of the symmetric part of σ yields the three principal components, $\sigma_{XX}$, $\sigma_{YY}$, and $\sigma_{ZZ}$. The isotropic shielding, $\sigma_{iso}$, is given by (1/3) Tr [σ]. The iso- tropic chemical shift, $\delta_{iso}$, is given by $\sigma_{ref} - \sigma_{iso}$, where $\sigma_{ref}$ is a reference shielding. Reference shieldings were determined by comparison of experimental chemical shifts for *L*-alanine with shieldings obtained from a calculation on a fully optimised crystal structure[7] (Cambridge Structural Database code LALNIN22). For $^{1}$H and $^{13}$C, reference shieldings were determined from the *y* intercept of a linear fit to the experimental shifts versus calculated shielding, with the gradient of the fit fixed to −1. Calculated shieldings for the three methyl protons were averaged to account for rapid rotation of the methyl group. Respective reference shieldings of 30.2 and 168.4 ppm were obtained for $^{1}$H and $^{13}$C. Calculated chemical shifts for the individual carbons in DABCO groups were averaged to account for the fast rotational dynamics of this group.

**S1.** Synthetic conditions for **1**⊃$AB_x$.

| Entry | Compound | General Formula [(a)] | Mass of **1** / g | Mass of *trans*-AB/ g | Loading time[(a)]/ h | Excess *trans*-AB removal [(b)]/ h |
|---|---|---|---|---|---|---|
| 1 | **1**⊃$AB_{1.0}$ | $[Zn_2(BDC)_2(DABCO)(AB)_{1.0}]$ | 0.3 | 0.30 | 6 | 3 |
| 2 | **1**⊃$AB_{0.9}$ | $[Zn_2(BDC)_2(DABCO)(AB)_{0.9}]$ | 0.3 | 0.08 | 6 | 0.5 |
| 3 | **1**⊃$AB_{0.5}$ | $[Zn_2(BDC)_2(DABCO)(AB)_{0.5}]$ | 0.3 | 0.06 | 6 | 0.5 |
| 4 | **1**⊃$AB_{0.3}$ | $[Zn_2(BDC)_2(DABCO)(AB)_{0.3}]$ | 0.3 | 0.04 | 6 | 0.5 |

[(a)] heated at 120 ˚C in a stoppered vial. [(b)] heated at 120 ˚C in an open vial under reduced pressure.

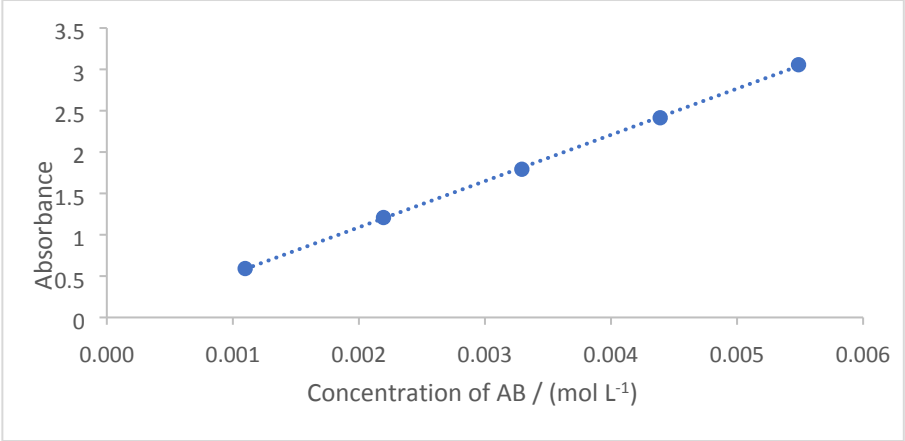


**S2**. UV/Vis calibration curve for known concentrations of *trans*-AB in MeOH.
UV-Vis data was collected on a Cary 60 UV/VIS spectrophotometer with a quartz cell (3 mL) within a 200-600 nm range. The peak absorbance at 441 nm was recorded for the calibration curve.

**S3.** Calculated masses of *trans*-AB for **1**⊃$AB_x$. (Absorbance at 441 nm)

| Sample | Absorbance/ abu | Mass of AB / g | Mass of sample/g | Mass of **1**/ g | Moles of **1** / mol | Moles of AB / mol | Ratio of AB/**1** |
|---|---|---|---|---|---|---|---|
| **1**⊃$AB_{1.0}$ | 0.801 | 0.014 | 0.055 | 0.041 | $7.15 \times 10^{-5}$ | $7.19 \times 10^{-5}$ | 0.99 |
| **1**⊃$AB_{0.9}$ | 0.677 | 0.011 | 0.051 | 0.040 | $6.88 \times 10^{-5}$ | $6.08 \times 10^{-5}$ | 0.88 |
| **1**⊃$AB_{0.5}$ | 0.461 | 0.008 | 0.053 | 0.046 | $7.90 \times 10^{-5}$ | $4.14 \times 10^{-5}$ | 0.52 |
| **1**⊃$AB_{0.3}$ | 0.280 | 0.005 | 0.050 | 0.045 | $7.75 \times 10^{-5}$ | $2.52 \times 10^{-5}$ | 0.32 |

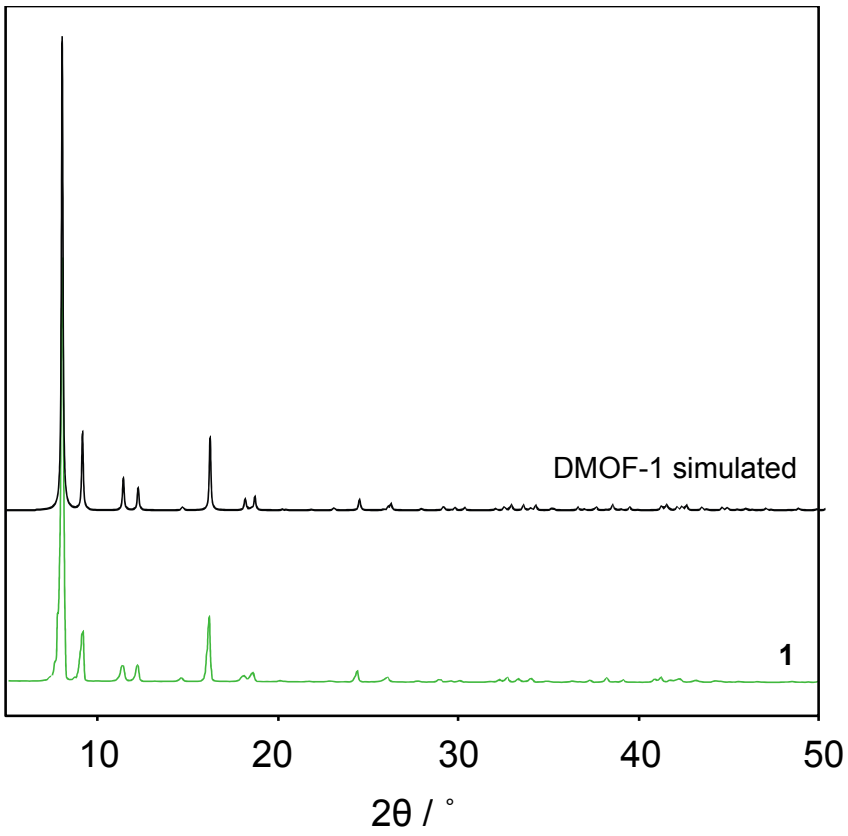


**S4.** XRPD patterns of simulated guest-free **1** (upper, based on the structure of Dybtsev *et al*.) and synthesised guest-free **1** (lower).[6]

**S5.** XRPD profile fits for of **1**⊃$AB_x$

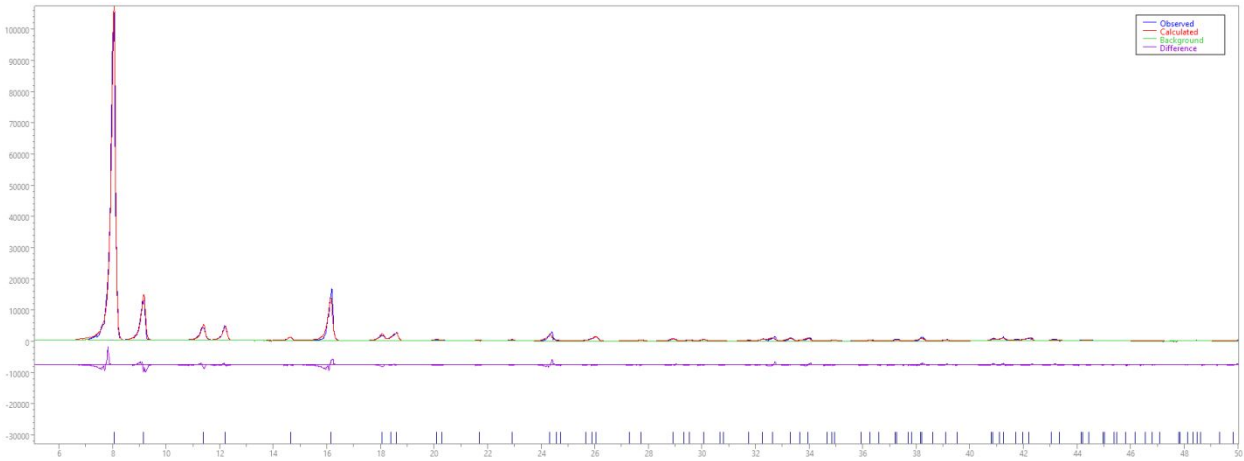


**S5a**) Le Bail fit of guest-free **1**. Indexing was carried out by N-TREOR09 on EXPO2014. The crystal system was found to be tetragonal. The lattice parameters were refined to be $a = b =$ 10.981(2) Å, $c$ = 9.654(1) Å, $\alpha=\beta=\gamma = 90^\circ$, V = 1162.6(7) Å$^3$. The space group was found to be *P*4/*mmm*. General formula $Zn_2C_{18}H_{16}N_4O_8$. The reliability (*R*) factor based on the powder profile *Rp* was 7.51 %.

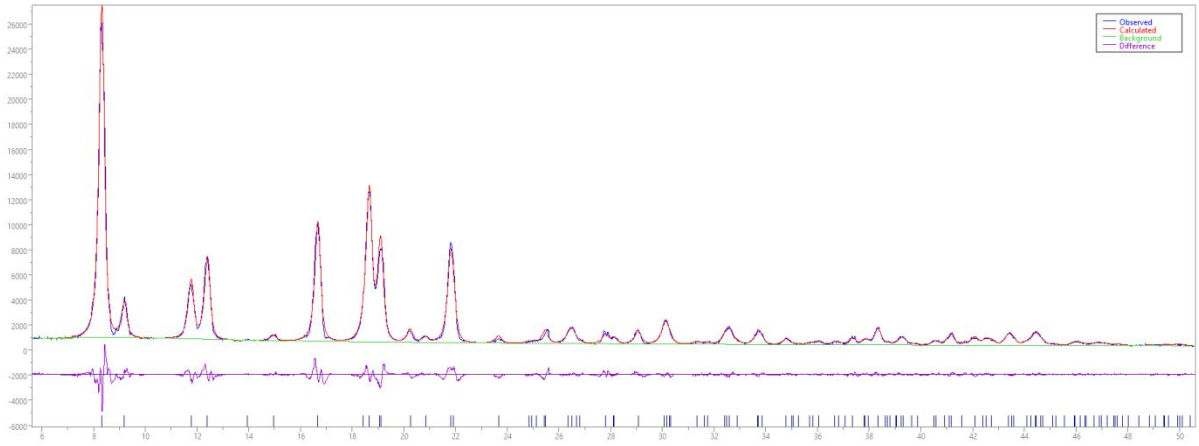


**S5b)** Le Bail fit of **1**⊃$AB_{1.0}$. The crystal system was found to be tetragonal. The lattice parameters were refined to be $a = b$ = 15.032(2) Å, $c$ = 19.276(3) Å, $\alpha = \beta = \gamma = 90°$, V = 4355.9(8) $Å^3$. The specific volume per $Zn_2$ unit is 1089.0 $Å^3$. The space group was found to be *I4/mcm*. General formula $Zn_2C_{18}H_{16}N_4O_8$. The reliability (R) factor based on the powder profile *Rp* was 5.64 %.

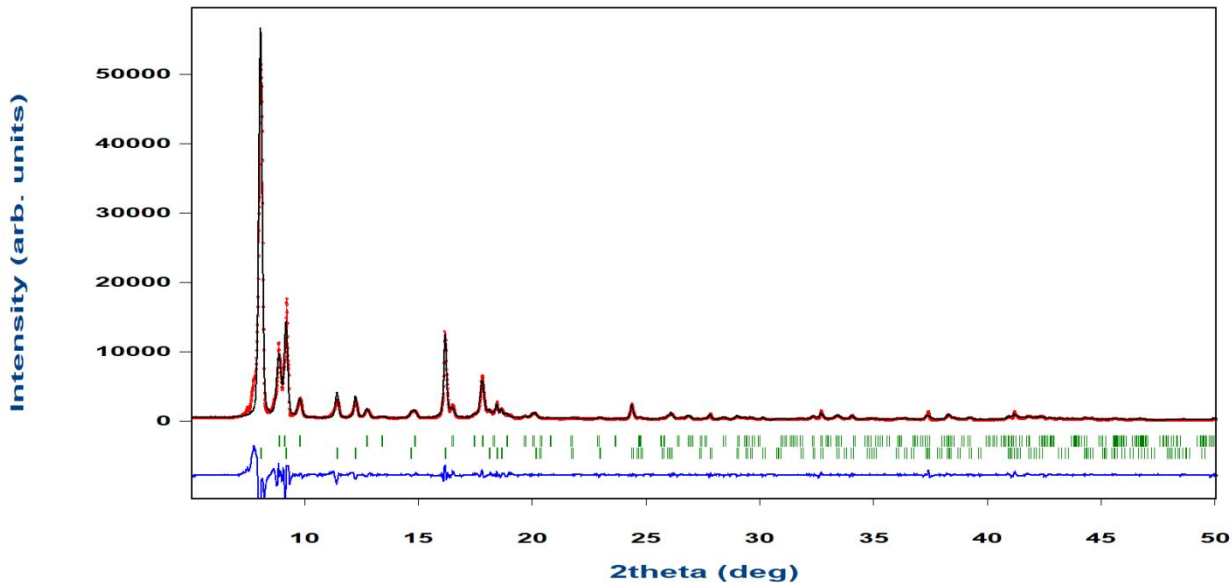


S**5c)** Le Bail fit of **1**⊃$AB_{0.3}$. The profile was fit with two phases. The first phase was found to be orthorhombic (*Cmmm*) with lattice parameters refined to be $a$ = 11.934(2) Å, $b$ = 18.044(4) Å, c = 9.692(4) Å, $\alpha. = \beta = \gamma = 90^{\circ}$. The second phase was tetragonal (*P4/mmm*) with lattice parameters refined to $a = b$ = 10.948(1) and $c$ = 9.616(1), $\alpha = \beta = \gamma = 90^{\circ}$. The reliability (*R*) factor based on the powder profile *Rp* is 11.11 %.

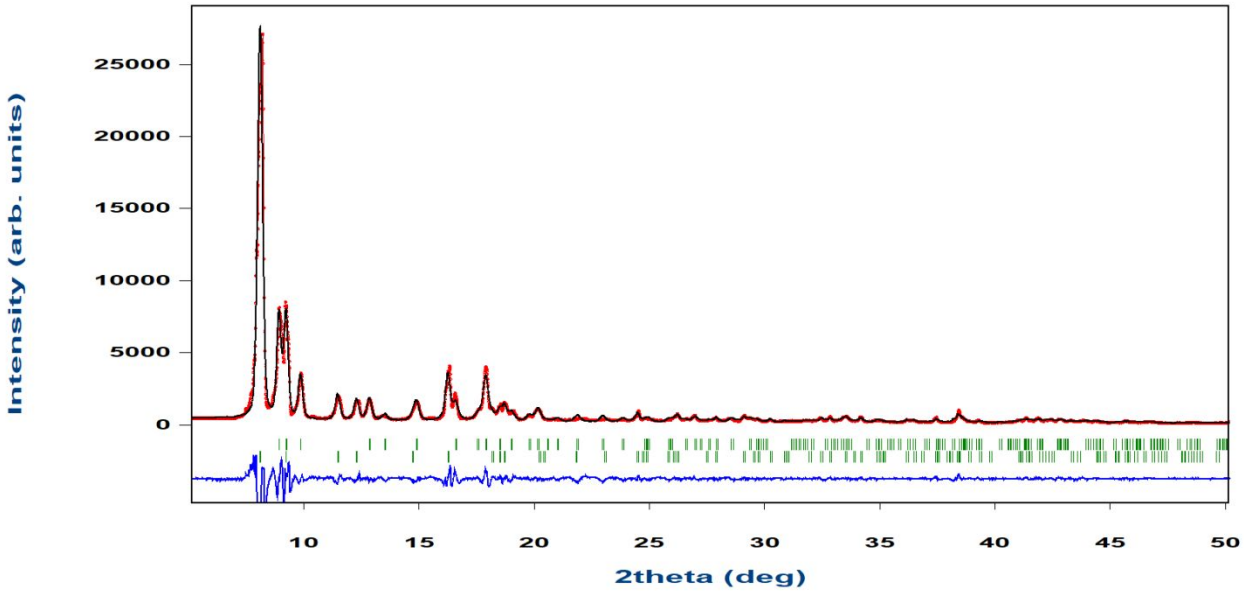


**S5d)** Le Bail fit of **1**⊃$AB_{0.5}$. The profile was fit with two phases. The first phase was found to be orthorhombic (*Cmmm*) with lattice parameters refined to be $a$ = 11.898(2) Å, $b$ = 17.951(4) Å, $c$ = 9.687(2) Å, $\alpha = \beta = \gamma = 90^{\circ}$. The second phase was tetragonal (*P4/mmm*) with lattice parameters refined to a = b = 10.910(2) and c = 9.610(2), $\alpha=\beta=\gamma = 90^{\circ}$. The reliability (*R*) factor based on the powder profile *Rp* is 7.23 %.

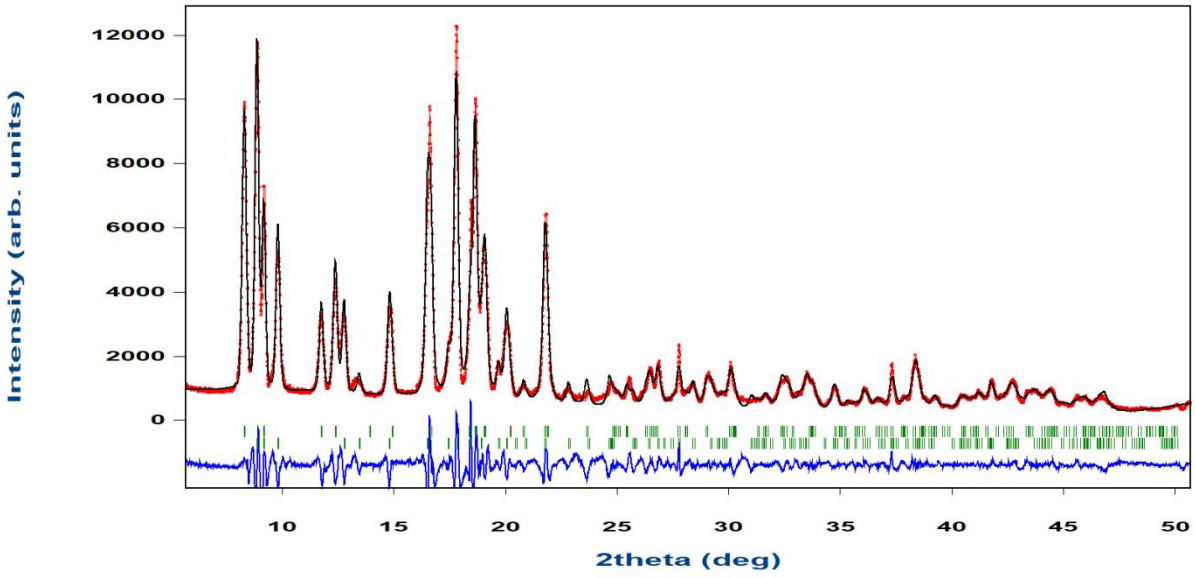


**S5e)** Le Bail fit of **1**⊃$AB_{0.9}$. The profile was fit with two phases. The first phase was found to be orthorhombic (*Cmmm*) with lattice parameters refined to be $a$ = 11.950(1) Å, $b$ = 18.021(2) Å, $c$ = 9.633(1) Å, $\alpha=\beta=\gamma = 90^{\circ}$. The second phase was tetragonal (*I4/mcm*) with lattice parameters refined to $a = b$ = 15.037(1) and $c$ = 19.280(3), $\alpha=\beta=\gamma = 90^{\circ}$. The reliability (*R*) factor based on the powder profile *Rp* is 12.43 %.

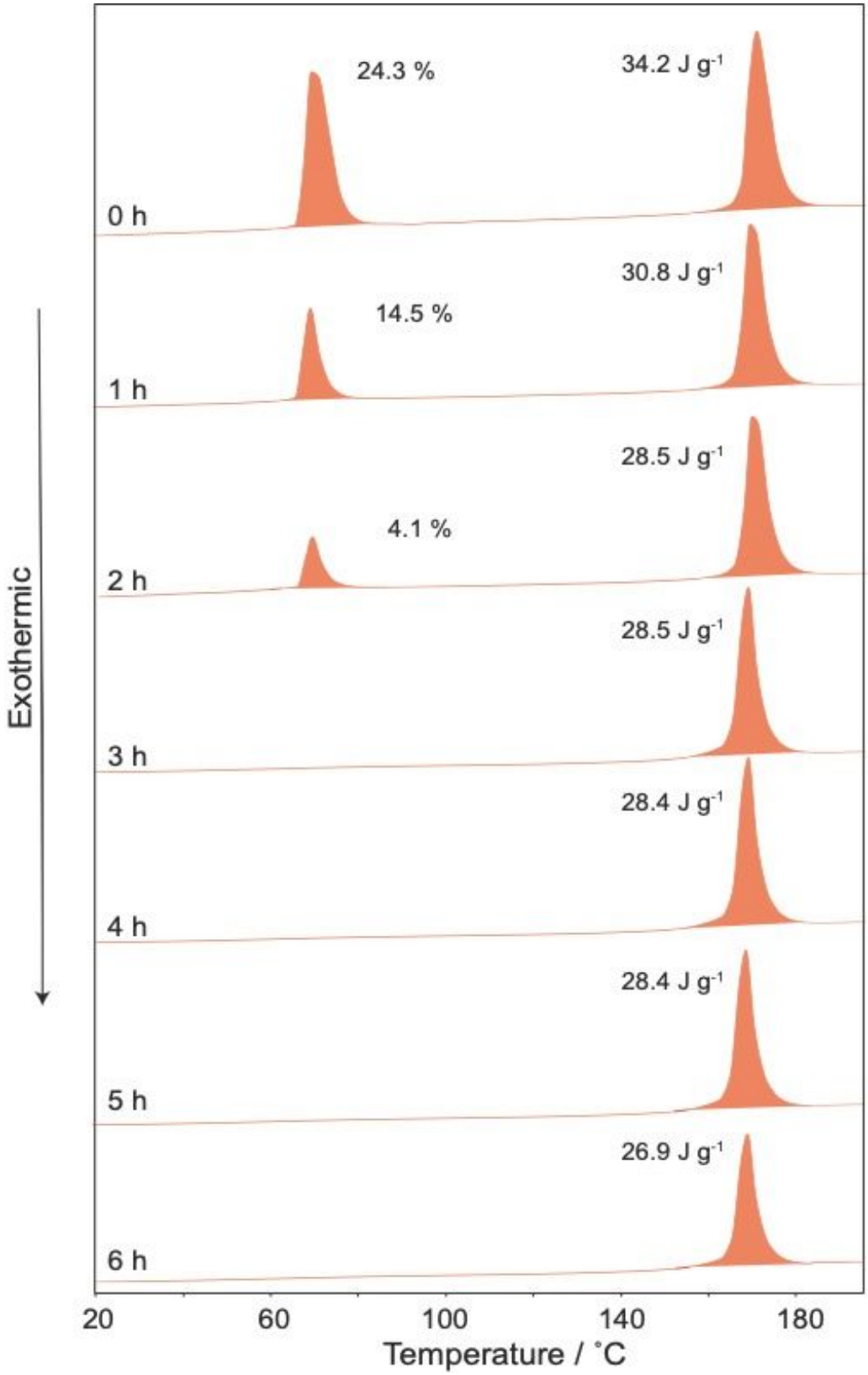


**S6.** DSC traces of the **1**⊃$AB_{1.0}$ with different durations of vacuum treatment at 120 ˚C. Between 0 – 2 hours crystalline *trans*-AB can be observed on the first heating branch and is fully removed after 3 h. The endothermic transition (1) energy stabilises after two hours before decreasing after six hours.

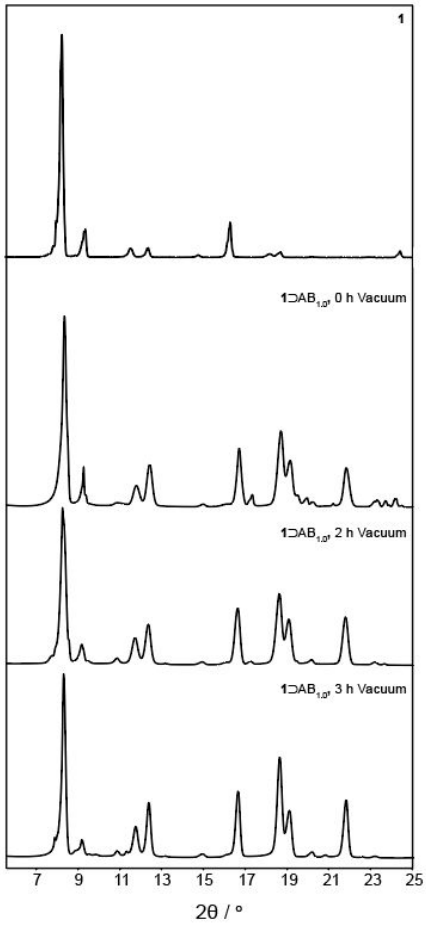


**S7.** XRPD patterns of **1**⊃$AB_{1.0}$ with different lengths of vacuum treatment at 120 ˚C.

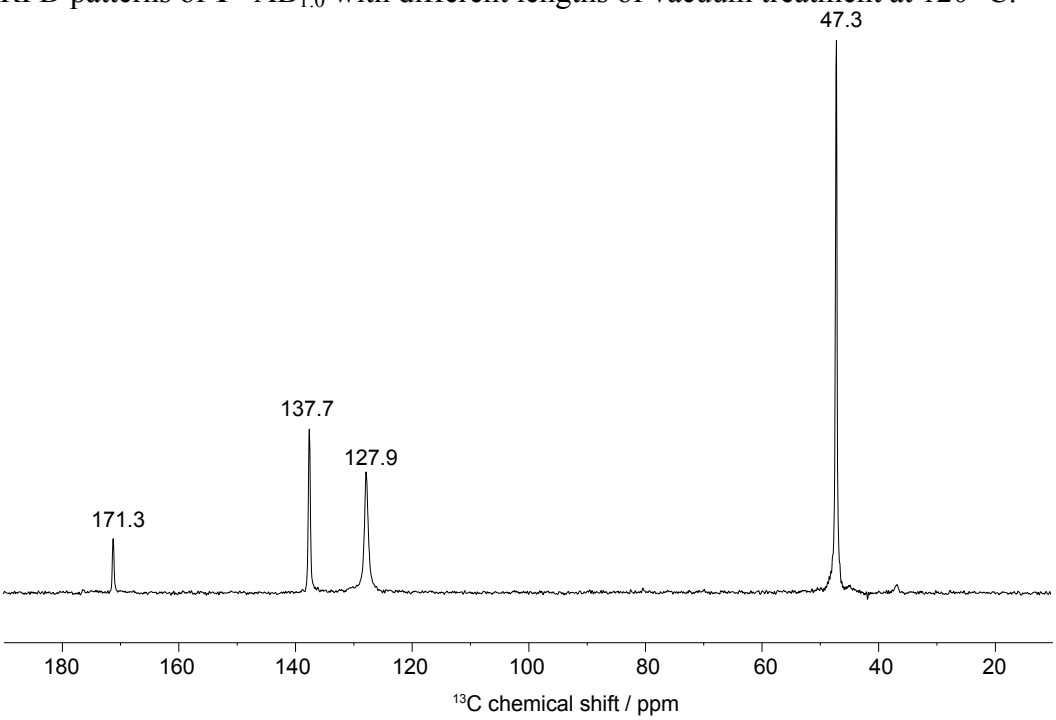


**S8**. $^{13}C$ CPMAS NMR spectrum of **1** recorded at 80 ˚C. The linewidth of the CH resonance at 127.9 ppm is significantly reduced compared to the spectrum recorded under ambient conditions in Figure 2.

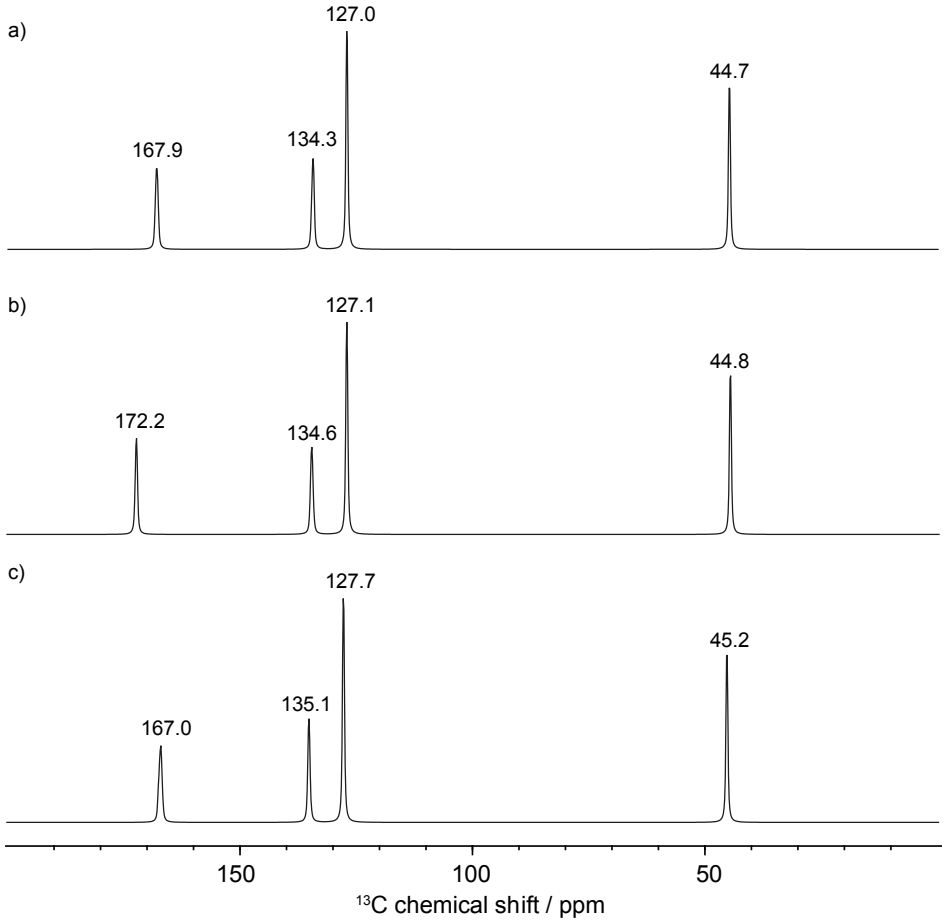


**S9**. Simulated $^{13}$C NMR spectra for "empty" **1** frameworks with fixed unit cell dimensions. a) *P*4/*mmm*; $a = b = 10.9288$ Å $c = 9.6084$ Å; $\alpha = \beta = \gamma = 90^{\circ}$. b) *Cmmm*; $a = 11.9640$ Å, $b = 18.065$ Å, $c = 9.6420$ Å; $\alpha = \beta = \gamma = 90^{\circ}$. c) *I*4/*mcm*; $a = b = 15.0630$ Å $c = 19.2470$ Å; $\alpha = \beta = \gamma = 90^{\circ}$. Calculated chemical shifts for the individual carbons in the DABCO group have been averaged to account for the fast rotational dynamics of this group.

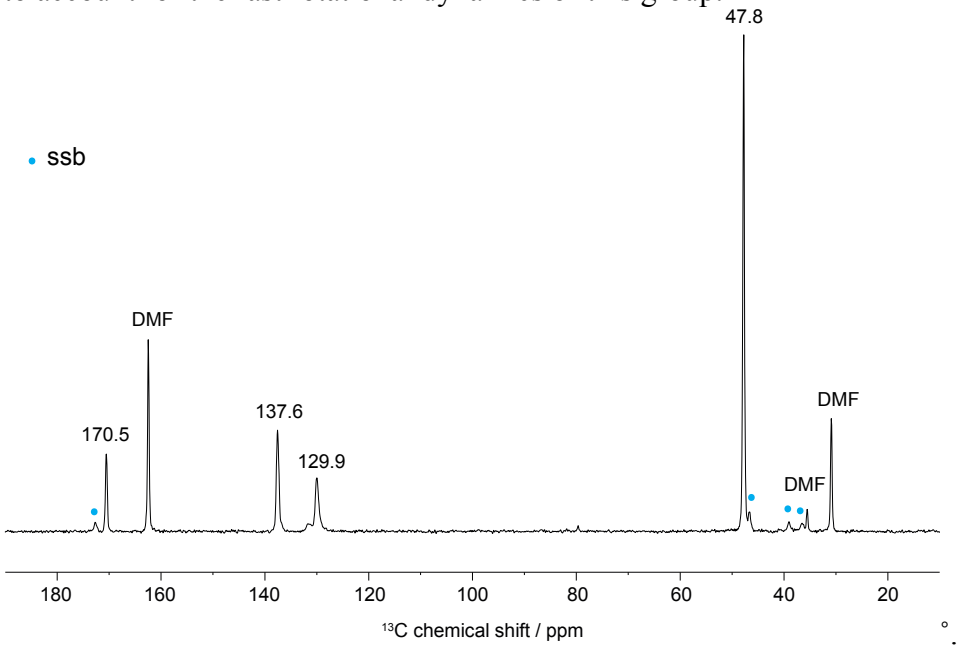


**S10.** $^{13}$C CPMAS NMR spectrum of **1**⊃DMF. Blue dots indicate spinning sidebands.

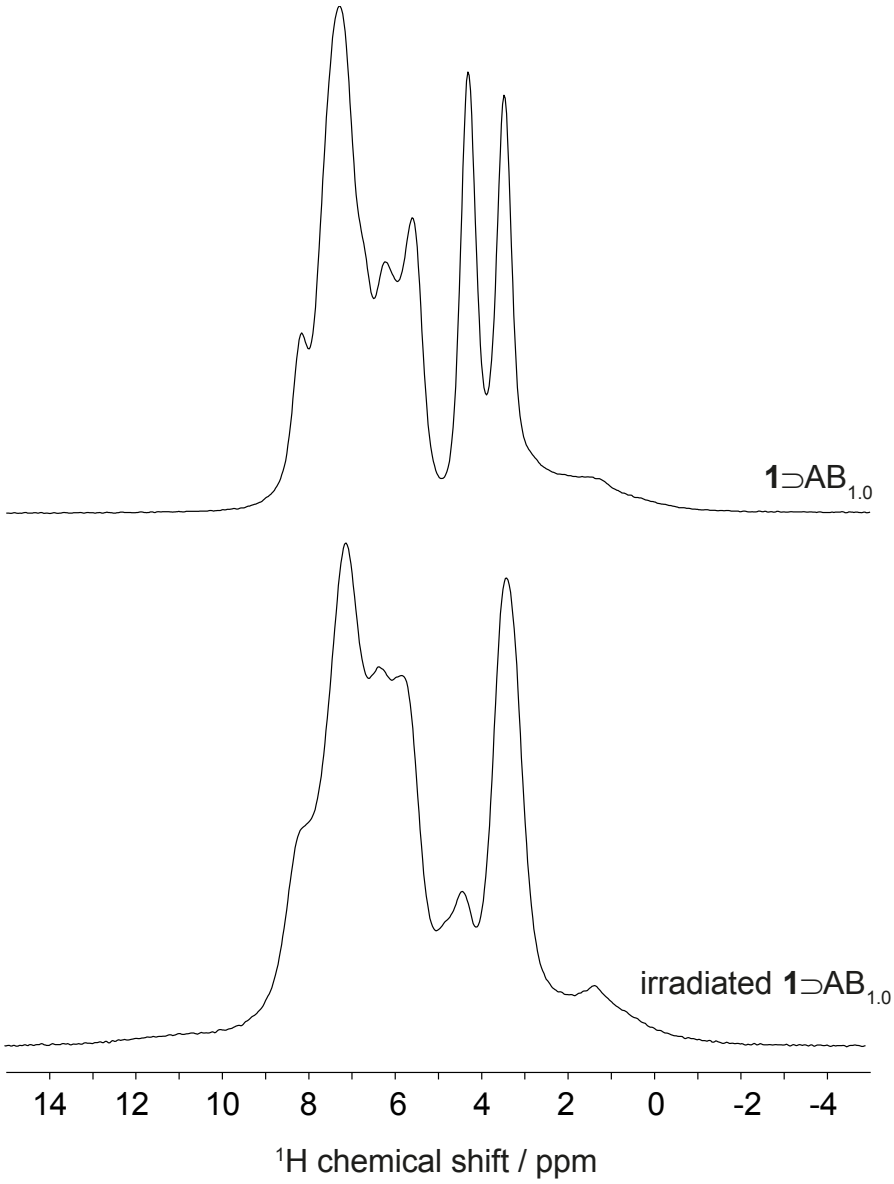


**S11.** Comparison of $^{1}$H MAS NMR of **1**⊃$AB_{1.0}$ (upper) and irradiated **1**⊃$AB_{1.0}$ (lower). Spectra were recorded at a magnetic field strength of 20.0 T at a MAS rate of 60 kHz.

**S12.** Experimental $^{13}C$ chemical shifts for *trans*-AB within **1**⊃$AB_{1.0}$ and calculated $^{13}C$ chemical shifts for a single molecule of *trans*-AB.

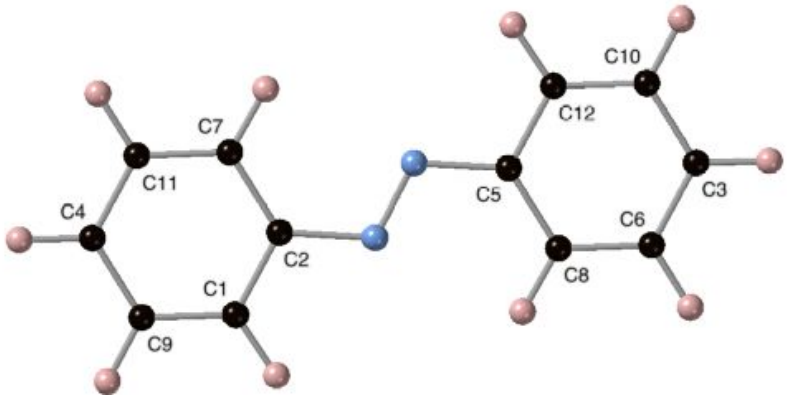


The calculated $^{13}C$ chemical shifts for a static molecule of *trans*-AB were not consistent with the resonances in **1**⊃$AB_{1.0}$. To model a *trans*-AB molecule which is undergoing pedal motion, chemically and positionally equivalent carbon atoms resonances were averaged. These include C1/C7, C9/C11, C8/C12 and C6/C10. The rotationally averaged model is consistent with the experimental chemical shifts (S12).

| C site | Calculated $^{13}C$ chemical shift static / ppm | Calculated $^{13}C$ chemical shift Rotational average /ppm | Experimental $^{13}C$ chemical shift /ppm |
|---|---|---|---|
| 1 | 134.4 | 122.2 | 123.8 |
| 2 | 152.5 | 152.5 | 151.8 |
| 3 | 130.0 | 130.0 | 129.5 |
| 4 | 129.8 | 129.8 | 129.5 |
| 5 | 152.4 | 152.4 | 151.8 |
| 6 | 126.6 | 126.8 | 127.0 |
| 7 | 109.9 | 122.2 | 123.9 |
| 8 | 109.8 | 122.0 | 122.8 |
| 9 | 127.0 | 126.8 | 127.0 |
| 10 | 127.0 | 126.8 | 127.0 |
| 11 | 126.7 | 126.8 | 127.0 |
| 12 | 134.2 | 122.0 | 122.8 |

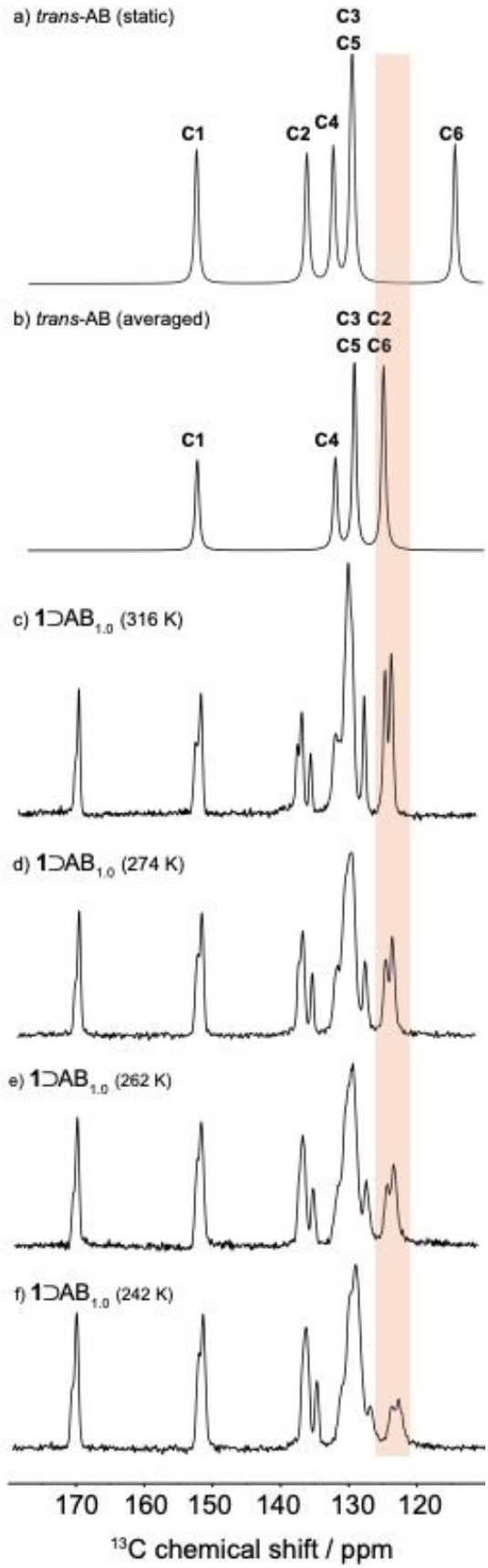


**S13**. Simulated $^{13}$C CPMAS NMR spectrum of a) a single molecule of *trans*-AB and b) a single molecule of *trans*-AB with chemical shifts averaged under the assumption of rotational motion of the rings or pedal motion of the central N=N bond. c-f) Experimental $^{13}$C CPMAS NMR spectra of **1**⊃$AB_{1.0}$ with decreasing temperature.

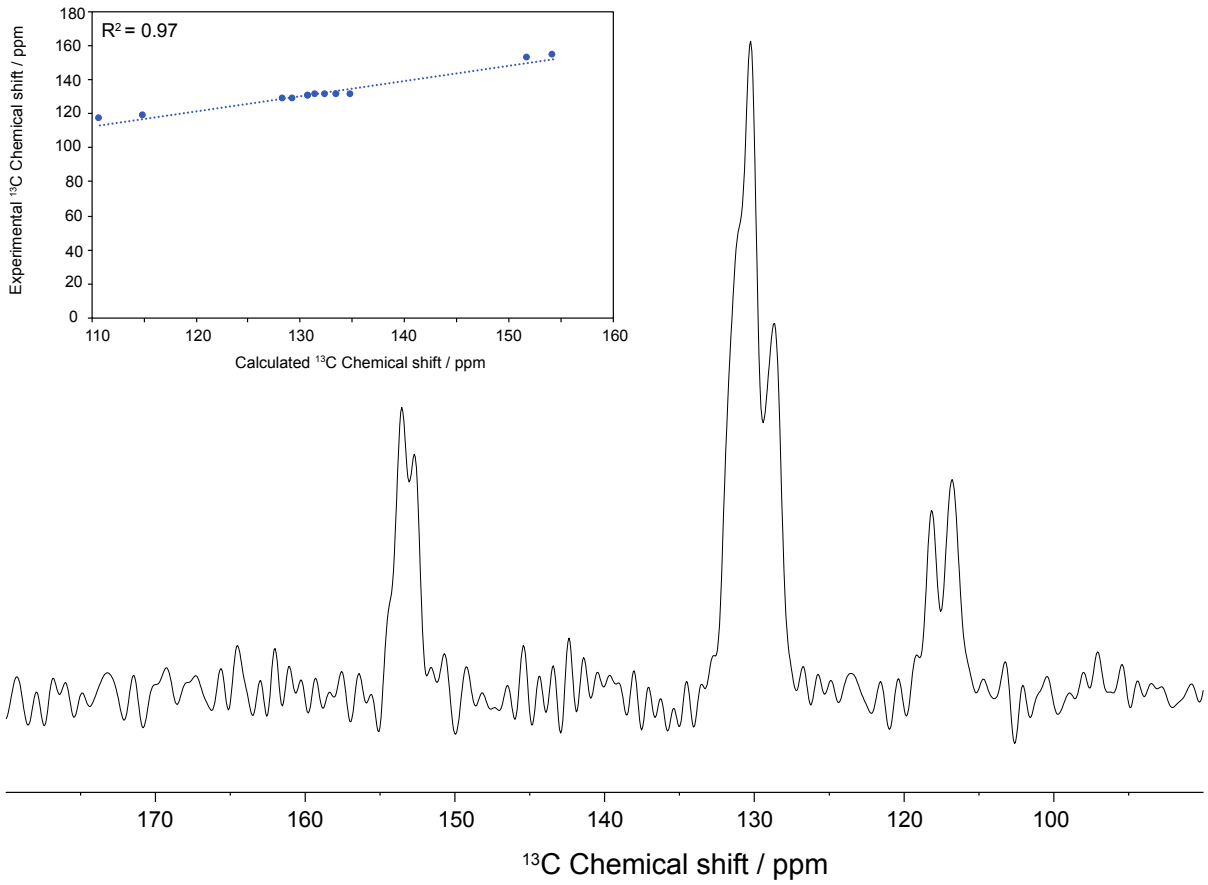


**S14.** $^{13}$C CPMAS NMR of crystalline *trans*-AB (inset- calculated $^{13}$C CP MAS NMR shifts v experimental *trans*-AB resonances).

**S15.** Calculated CPMAS NMR $^{13}$C chemical shifts for crystalline *trans*-AB.

| C Site | Calculated $^{13}$C chemical shift / ppm | Experimental $^{13}$C chemical shift / ppm |
|---|---|---|
| 1 | 110.8 | 116.8 |
| 2 | 115.1 | 118.2 |
| 3 | 128.4 | 128.7 |
| 4 | 129.5 | 128.7 |
| 5 | 130.9 | 130.3 |
| 6 | 130.9 | 130.3 |
| 7 | 131.5 | 131.1 |
| 8 | 132.5 | 131.1 |
| 9 | 133.6 | 131.1 |
| 10 | 134.9 | 131.1 |
| 11 | 152.0 | 152.7 |
| 12 | 154.4 | 153.6 |

**S16**. Determination of the decrease in activation energy for rotational motion upon confinement.

The calculated chemical shift difference between the C2 and C6 carbons in azobenzene is 24.5 ppm. At a $^{13}C$ Larmor frequency of 176 MHz, this corresponds to a frequency difference, $\Delta\nu$, of 4.312 kHz. If rotational dynamics take place (either by rotation of the phenyl ring around the N=N bond, or by pedal motion of the N=N bond itself) the C2 and C6 carbons will undergo chemical exchange leading to motional broadening of the resonances. The resonances coalesce into a single resonance when the rate of chemical exchange, $k$, is equal to $(p/\sqrt{2})\Delta\nu = 9.578$ kHz.

For crystalline azobenzene, the rate constant for dynamic pedal motion of the N=N linkage, $k_{cryst}$, has been estimated to be on the order of 100 Hz. Given that separate resonances for C2 and C6 are not observed at the expected shifts in the ambient-temperature $^{13}C$ CPMAS NMR spectrum of **1**⊃$AB_{1.0}$ (Fig. 2 in the main text), it is assumed that these have coalesced due to rotational dynamics with a rate constant, $k_{occl}$, that is at least 9.578 kHz. Under the assumption that pedal motion is responsible for these rotational dynamics, the difference in activation energy for motion in the two cases, $E_a^{occl} - E_a^{cryst}$, can be estimated according to first-order Arrhenius kinetics using

$$ln\left(\frac{k_{cryst}}{k_{occl}}\right) = \frac{E_a^{occl} - E_a^{cryst}}{RT}$$

where $R$ is the ideal gas constant and $T$ is temperature (assumed to be 298 K).

Using this approach, $E_a^{occl} - E_a^{cryst}$ is found to be 11.303 kJ mol$^{-1}$.

**S17.** DSC data for **1**⊃$AB_x$ over the first heating/cooling cycle.

| Compound | Endothermic (1) transition / J g$^{-1}$ | Endothermic (1) transition range / ˚C | Exothermic (1) / J g$^{-1}$ | Exothermic (1) transition range / ˚C |
|---|---|---|---|---|
| **1**⊃$AB_{1.0}$ | 28.4 | 30 | 28.0 | 30 |
| **1**⊃$AB_{0.9}$ | 25.0 | 22 | 24.8 | 22 |
| **1**⊃$AB_{0.5}$ | 12.9 | 18 | 12.7 | 20 |
| **1**⊃$AB_{0.3}$ | 5.1 | 15 | 5.0 | 18 |

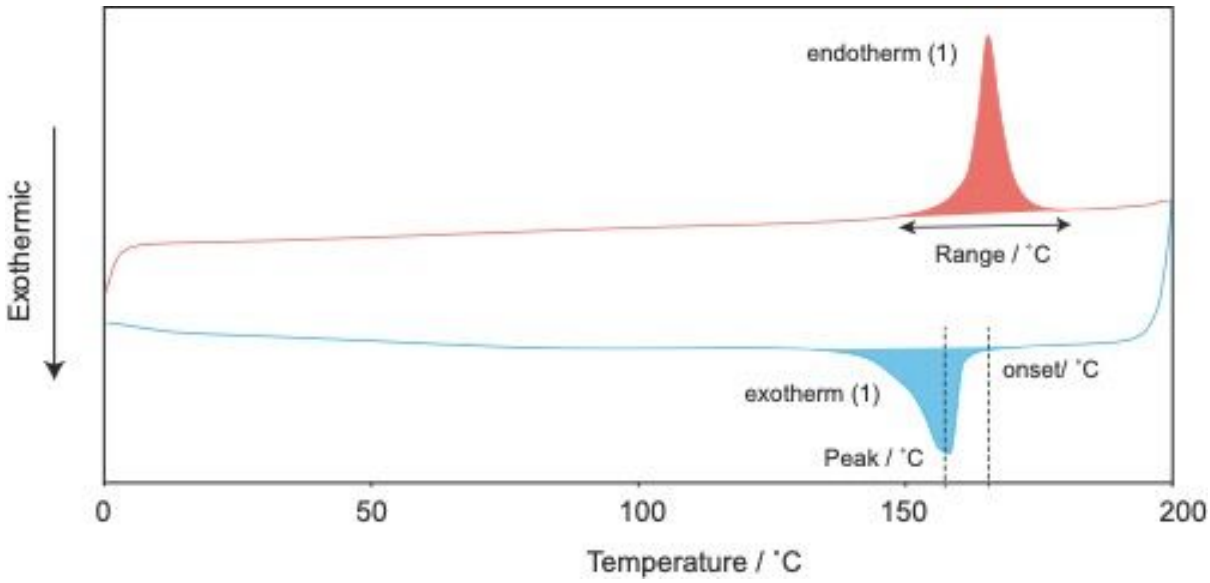


Key - DSC cycle for **S17** and **S18**. First heating branch (orange). First cooling branch (blue).

**S18a.** Convergence of endothermic peak and exothermic peak position for **1**⊃$AB_{1.0}$ at different heating rates. Endothermic (1) transition (Blue), Exothermic (1) transition (yellow).

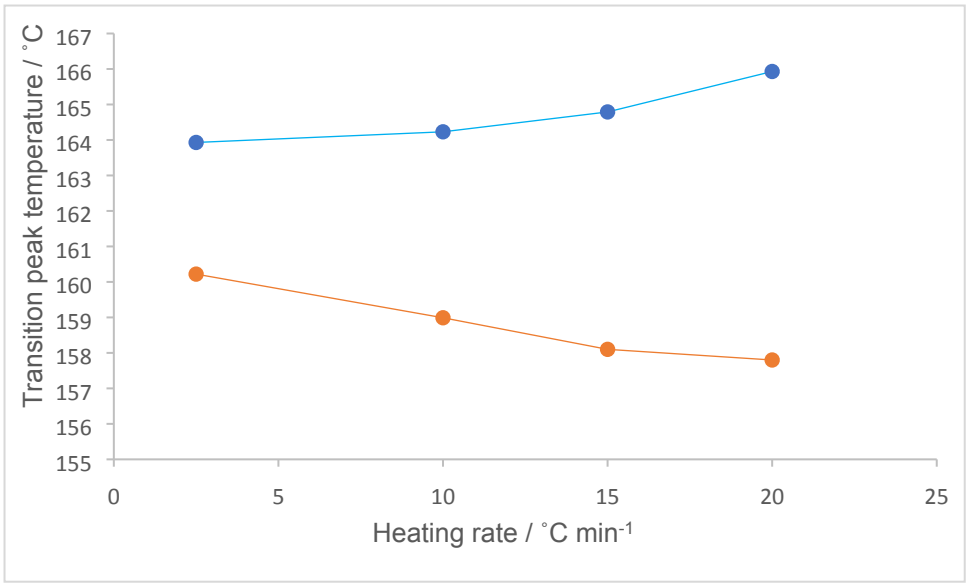


**S18b.** Peak positions for endothermic (1) and exothermic (1) transitions for **1**⊃$AB_{1.0}$ at different heating rates.

| Heating Rate / ˚C $min^{-1}$ | Endotherm (1) peak / ˚C | Exotherm (1) peak / ˚C | Δ/ ˚C |
|---|---|---|---|
| 2.5 | 163.9 | 160.2 | 3.7 |
| 10 | 164.2 | 158.9 | 5.2 |
| 15 | 164.8 | 158.1 | 6.7 |
| 20 | 165.9 | 157.8 | 7.4 |

**S18c.** Onset temperatures for endothermic (1) and exothermic (1) transitions for **1**⊃$AB_{1.0}$ at different heating rates.

| Heating Rate / ˚C $min^{-1}$ | *Endotherm (1)* onset / ˚C | *Exotherm (1)* onset / ˚C | Δ/ ˚C |
|---|---|---|---|
| 2.5 | 161.1 | 159.7 | 1.4 |
| 10 | 161.0 | 162.4 | -1.4 |
| 15 | 161.3 | 161.2 | 0.1 |
| 20 | 161.6 | 161.8 | -0.2 |

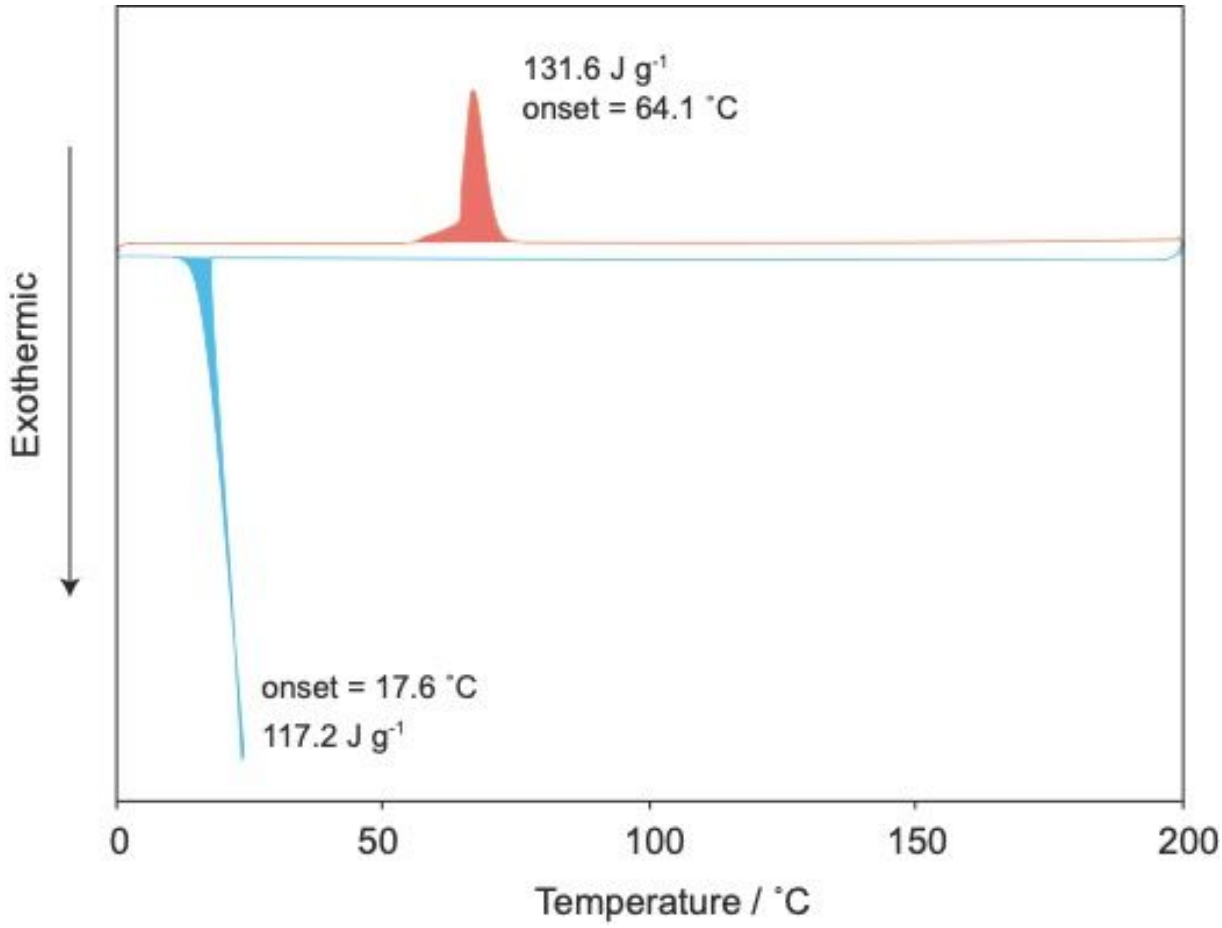


**S19.** DSC cycle of crystalline *trans*-AB. First heating branch, 0-200 ˚C, 20 ˚C $min^{-1}$ (orange). First cooling branch, 200-0 ˚C, -20 ˚C $min^{-1}$ (blue).

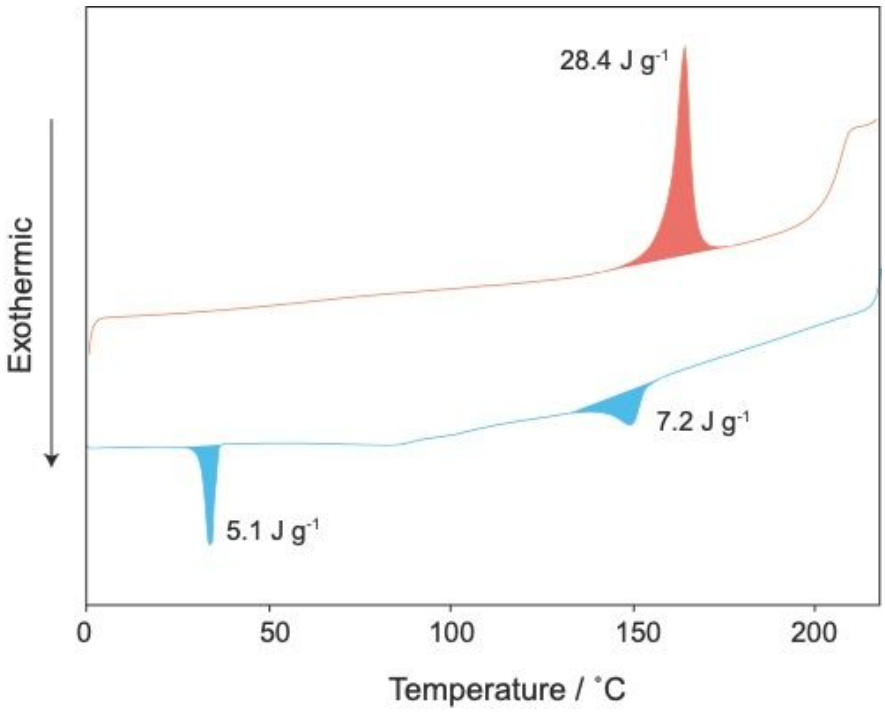


**S20**. DSC cycle for **1**⊃$AB_{1.0}$. First heating branch, 0 -220 ˚C, 20 K $min^{-1}$ (orange). First cooling branch, 220 – 0 ˚C, -20 ˚C $min^{-1}$ (blue).

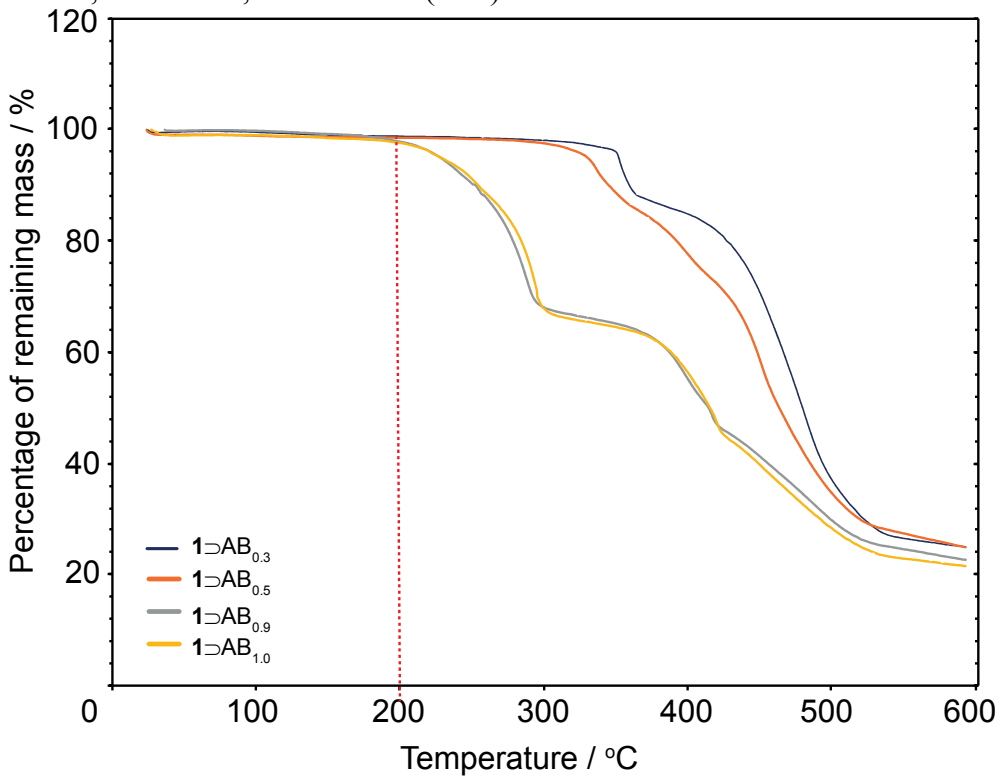


**S21.** TGA of **1**⊃$AB_x$. The final masses are consistent with the percentage loading of trans-AB in each composite and expected degradation product. The percentage of remaining mass is stable between 25 – 225 ˚C between 100 – 98.5 % for each of the composites. The 35 – 38% mass loss between 220 ˚C and 380 ˚C for **1**⊃$AB_{1.0}$ and **1**⊃$AB_{0.9}$ is consistent with the loss of *trans*-AB and DABCO before the full collapse of the MOF structure.

**S22.** VT-XRPD patterns and profile fittings of **1**⊃$AB_{1.0}$ between 25 – 180 °C.

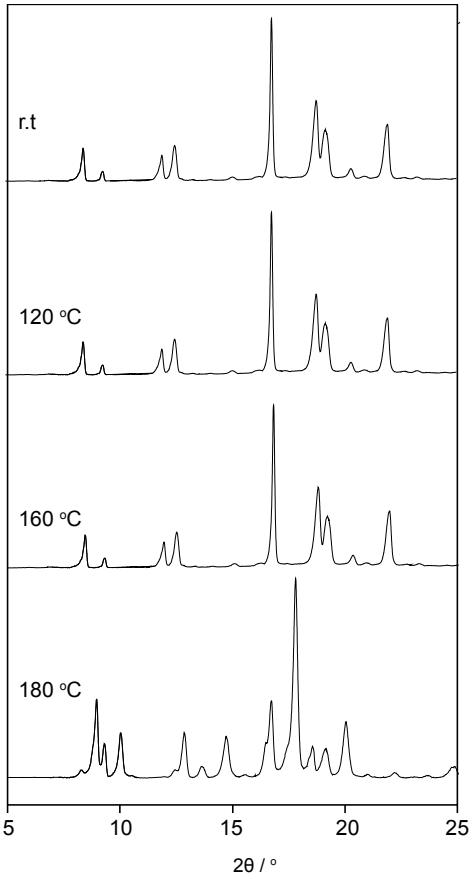


**S22a)** VT-XRPD patterns of **1**⊃$AB_{1.0}$ between room temperature and 180 °C.

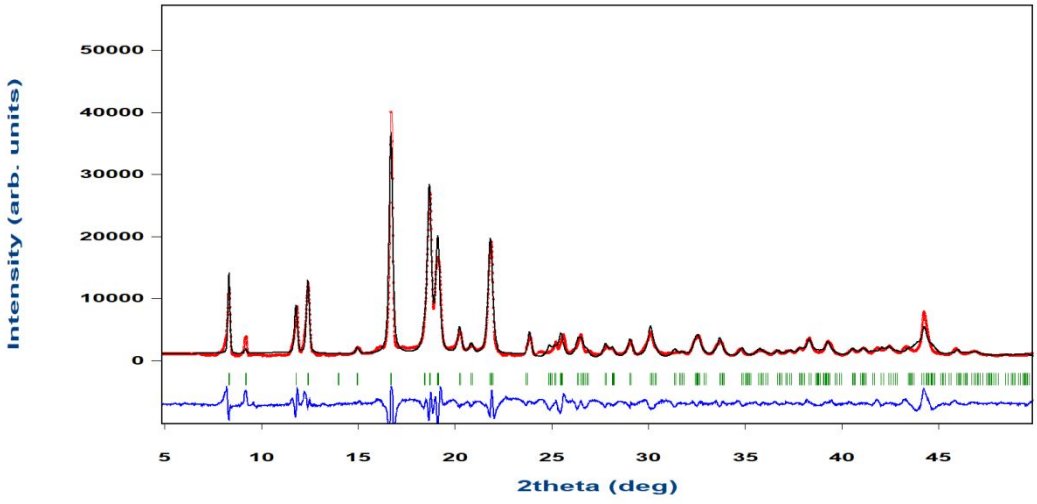


**S22b)** Le Bail fit of **1**⊃$AB_{1.0}$ at 160 °C. The crystal system was found to be tetragonal in the *I*4/*mcm* space group. The lattice parameters were refined to be $a = b = 15.030(2)$ Å, $c = 19.234(3)$ Å, $\alpha = \beta = \gamma = 90°$.The unit cell parameters and space group are consistent with **1**⊃$AB_{1.0}$ at room temperature. The reliability (*R*) factor based on the powder profile *Rp* is 11.58 %.

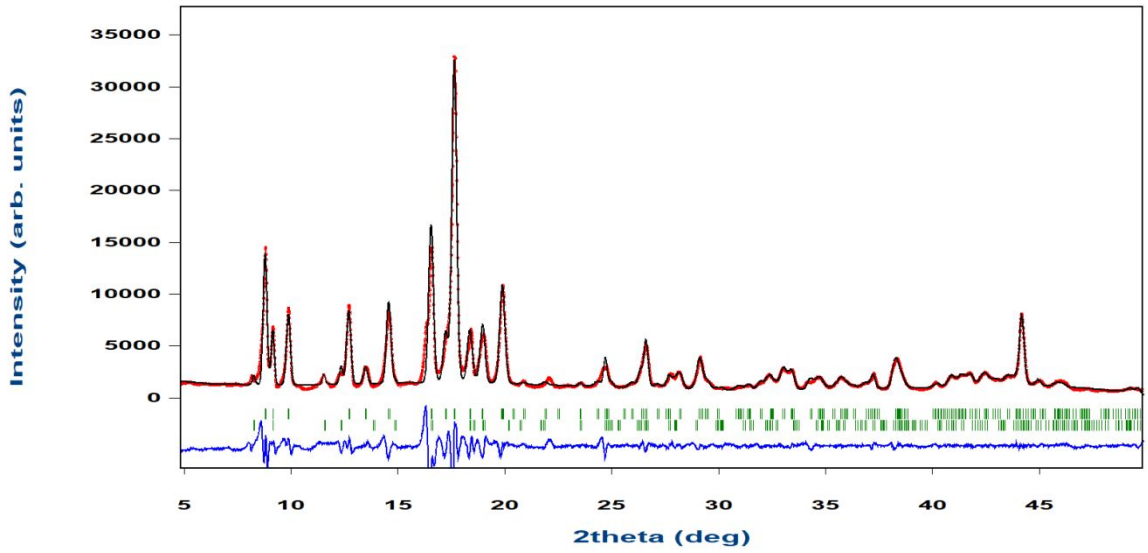


**S22c)** Le Bail fit of **1**⊃$AB_{1.0}$ at 180 °C. The crystal system was found to be orthorhombic in the *Cmmm* space group. The lattice parameters were refined to be $a$ = 12.154(1) Å, $b$ = 17.894(2) Å, $c$ = 9.661(1) Å, $\alpha = \beta = \gamma = 90°$. Residual reflections from the tetragonal phase at 160 ˚C are fitted with unit cell parameters of $a = b$ = 15.031(1) Å, $c$ = 19.242(3) Å, $\alpha = \beta = \gamma = 90°$. in the *I4/mcm* space group. The reliability ($R$) factor based on the powder profile *Rp* is 8.91 %.

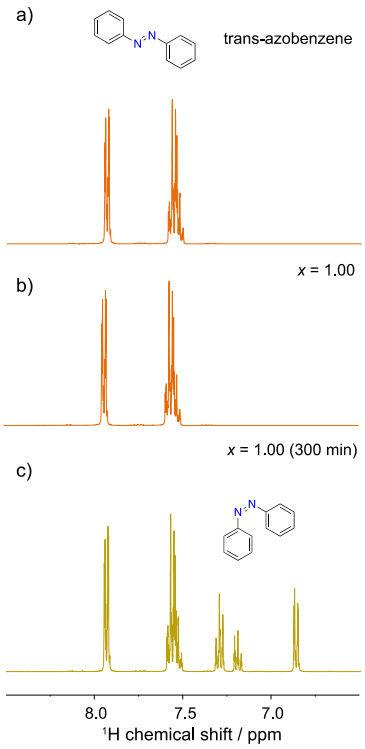


**S23.** $^1$H NMR spectra of a) *trans*-AB, b) Extract from **1**⊃$AB_{1.0}$ showing characteristic *trans*-AB resonances, c) Extract from irradiated **1**⊃$AB_{1.0}$ showing both *trans*-AB and *cis*-AB resonances. Measured in MeOH-$_{d4}$.

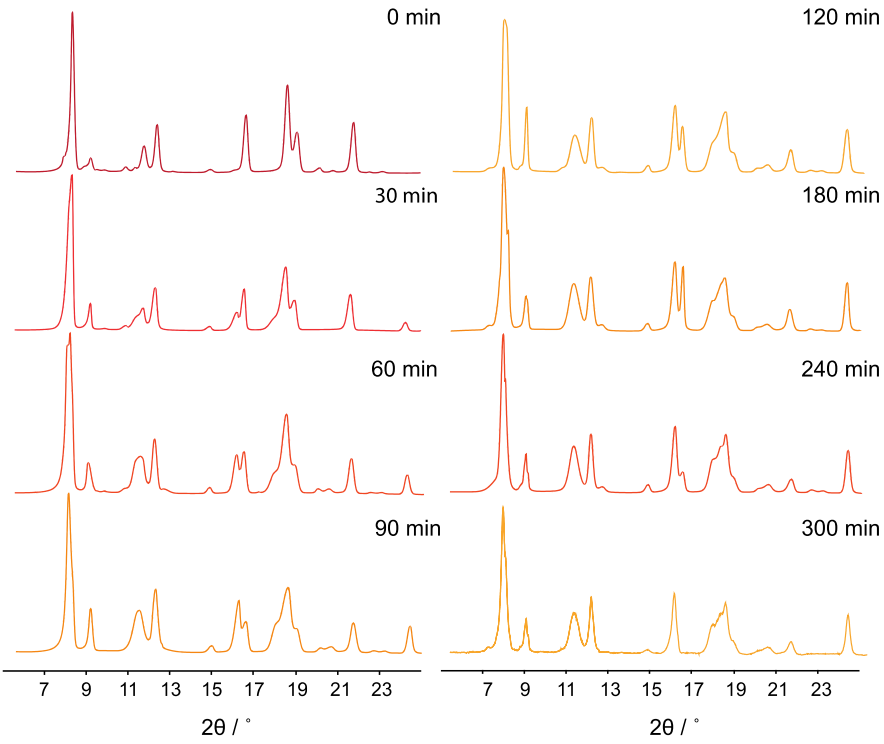


**S24.** XRPD patterns and profile fits for **1**⊃$AB_x$ fits which has been irradiated with UV light between 0 – 300 minutes.

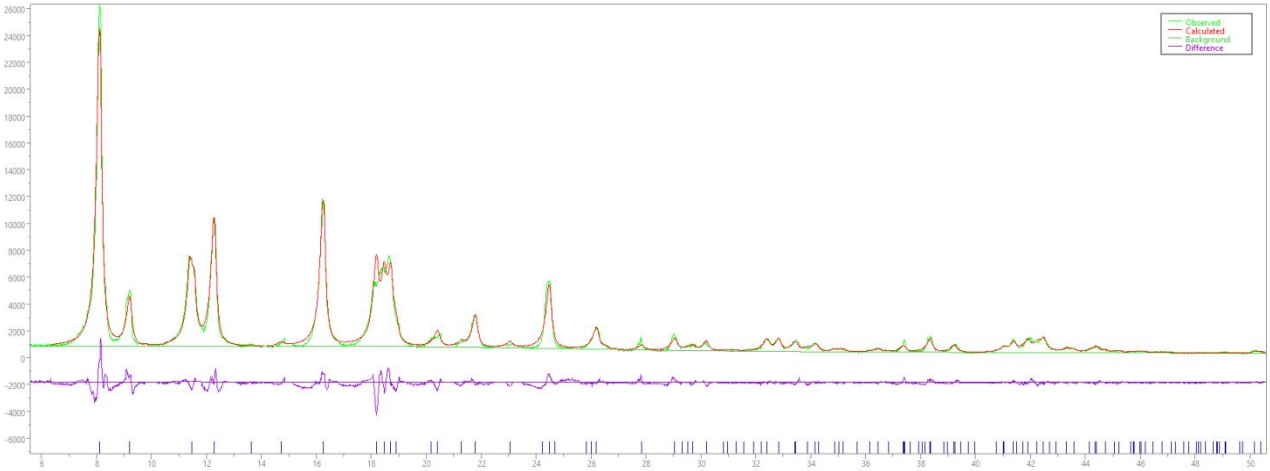

**S24a)** Le Bail fit of **1**⊃$AB_{1.0}$ after 300 minutes of irradiation. Indexing was carried out by N-TREOR09 on EXPO2014. The crystal system was found to be tetragonal in the *I4/mcm* space group. The lattice parameters were refined to be $a = b$ = 15.412(1) Å, $c$ = 19.113(3), Å, $\alpha = \beta = \gamma = 90^\circ$, V = 4539.8(9) Å$^3$. The specific volume per $Zn_2$ unit is 1134.4 Å$^3$. General formula $Zn_8C_{128}H_{120}N_{16}O_{32}$. The reliability ($R$) factor based on the powder profile $Rp$ is 8.91 %.

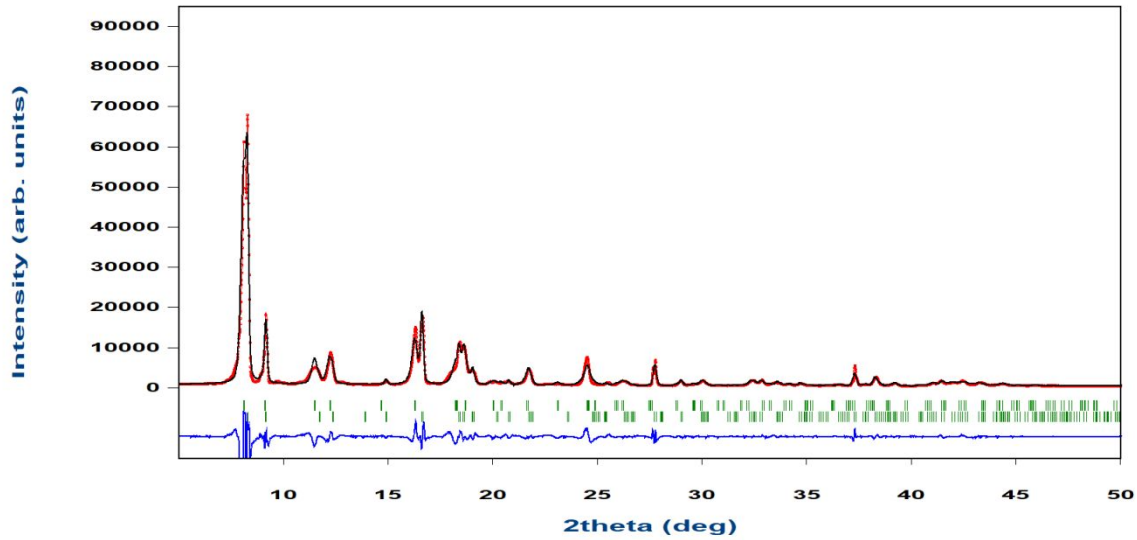


**S24b)** Le Bail fit of **1**⊃$AB_{0.9}$ after 300 minutes of irradiation. The profile was fit with two phases. The first phase was found to be tetragonal (*P4/mmm*) with lattice parameters refined to be $a = b$ = 10.980(2) Å, $c$ = 9.653(3) Å, $\alpha = \beta = \gamma = 90^{\circ}$. The second phase was tetragonal (*I4/mcm*) with lattice parameters refined to $a = b$ = 15.034(2) Å and c = 19.320(2) Å, $\alpha = \beta = \gamma = 90^{\circ}$. The reliability (*R*) factor based on the powder profile *Rp* is 9.77 %.

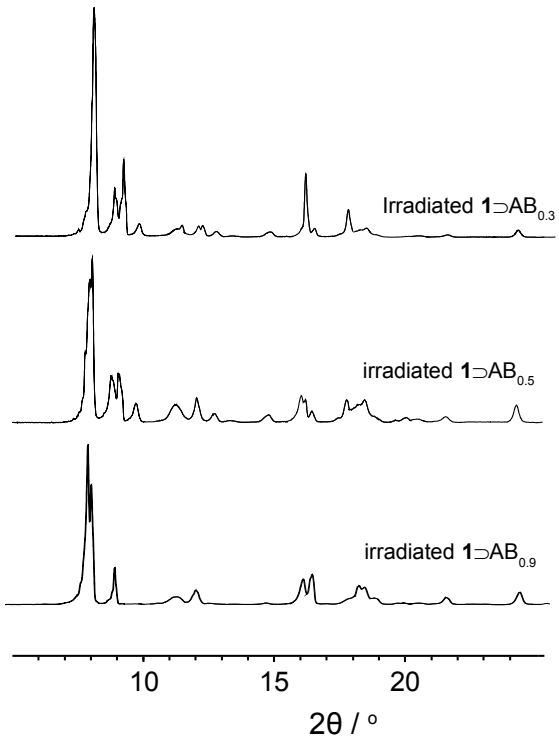


**S24c)** XRPD for **1**⊃$AB_x$ which has been irradiated with UV light for 300 minutes.

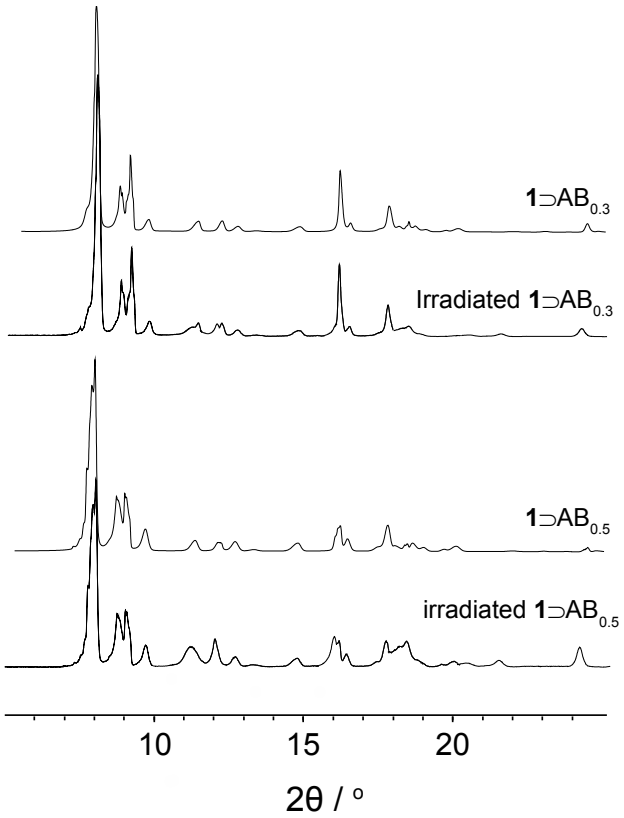


**S24d)** Comparison between pre-irradiated and irradiated forms of **1**⊃$AB_{0.3}$ and **1**⊃$AB_{0.5.}$ The new reflections were too small to accurately index.

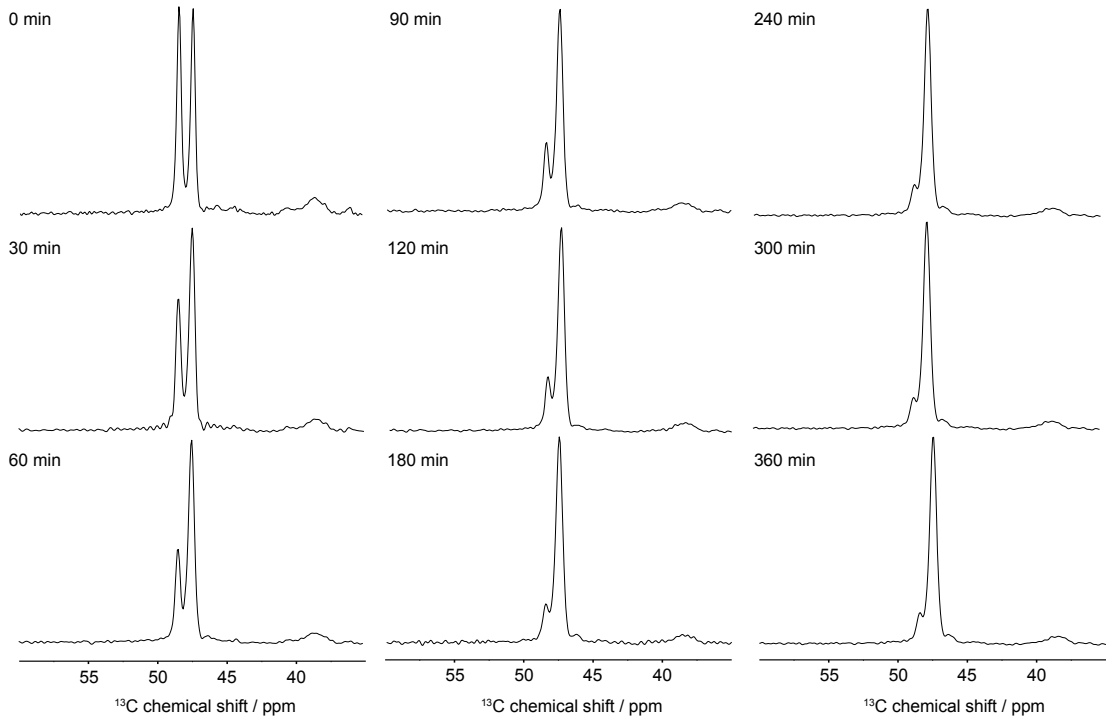


**S25**. $^{13}C$ CPMAS NMR of **1**⊃$AB_{1.0}$ showing the change in the DABCO resonance during irradiation with UV light.

**S26.** $^{13}C$ CPMAS NMR of **1**⊃$AB_{1.0}$ showing the change in the aromatic resonances during irradiation

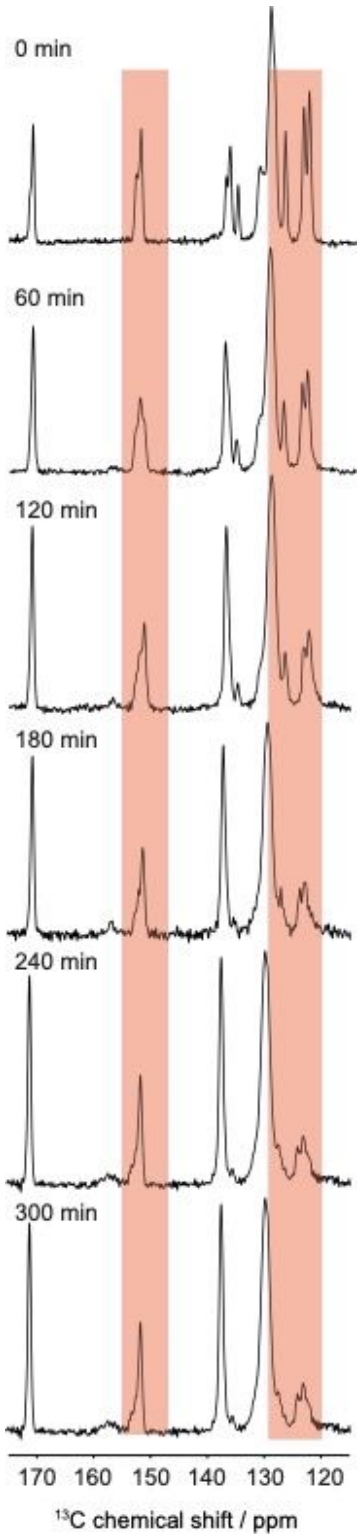

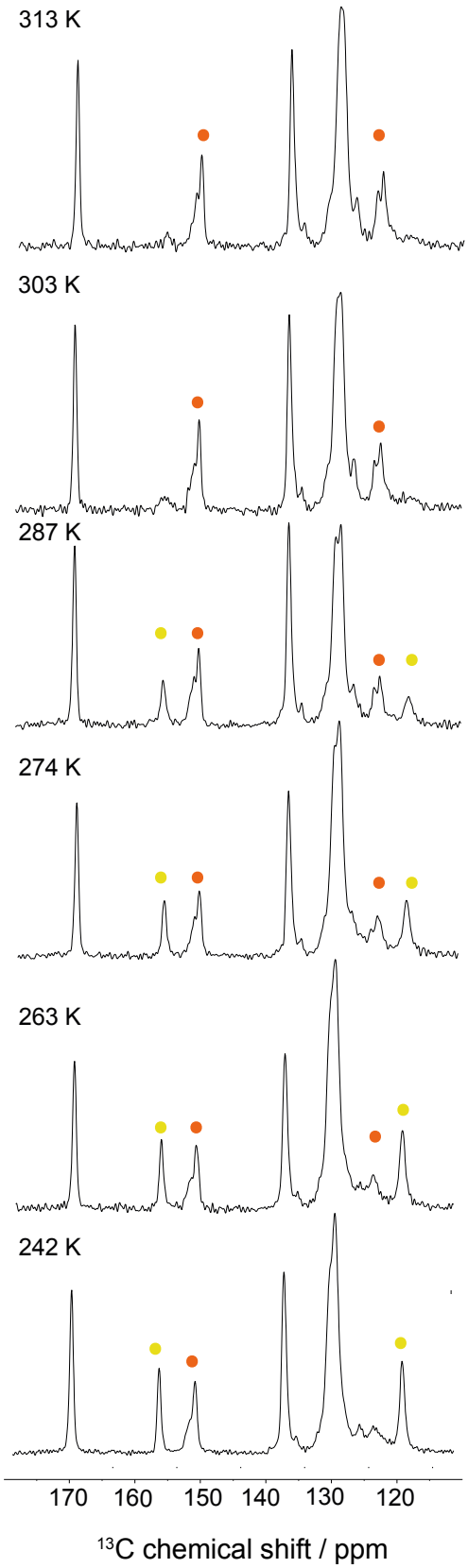


**S27.** $^{13}$C CPMAS NMR of irradiated **1**⊃$AB_{1.0}$ (110-175 ppm) showing the change in the aromatic resonances during a reduction in temperature. Characteristic *trans*-AB resonances (orange) and *cis*-AB resonances (yellow).

**S28.** Experimental $^{13}C$ chemical shifts for *cis*-AB within **1**⊃$AB_{1.0}$ at 242 K and calculated $^{13}C$ chemical shifts of a single molecule of *cis*-AB.

| C site | Calculated $^{13}C$ chemical shift (static) / ppm | Calculated $^{13}C$ chemical shift (rotational average) / ppm | Experimental $^{13}C$ chemical shift / ppm |
|---|---|---|---|
| 1 | 126.9 | 118.7 | 118.6 |
| 2 | 125.2 | 125.9 | 129.2 |
| 3 | 110.7 | 118.7 | 118.6 |
| 4 | 154.8 | 155.4 | 156.8 |
| 5 | 126.3 | 127.0 | 129.2 |
| 6 | 125.9 | 118.7 | 118.6 |
| 7 | 125.7 | 127.0 | 129.2 |
| 8 | 125.1 | 126.0 | 125.4 |
| 9 | 127.9 | 127.0 | 129.2 |
| 10 | 111.2 | 118.7 | 118.6 |
| 11 | 156.0 | 155.4 | 156.8 |
| 12 | 127.9 | 127.0 | 125.4 |

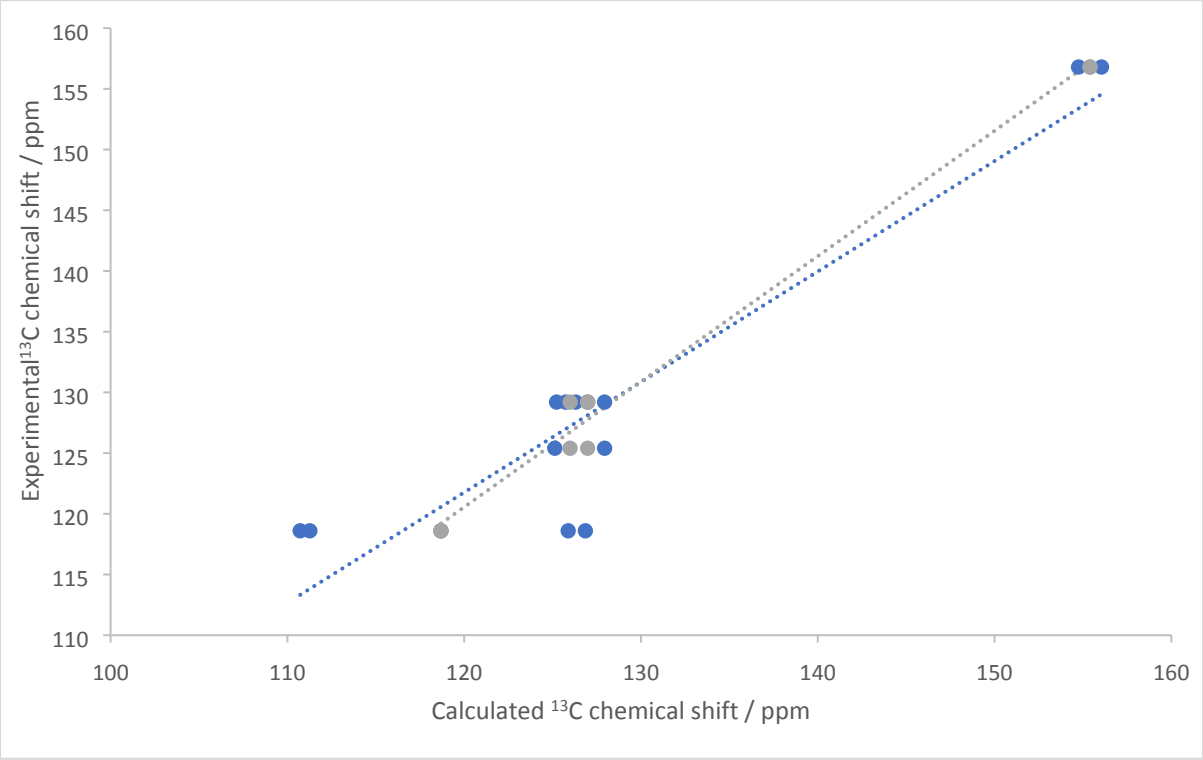


**S29**. Experimental $^{13}C$ chemical shifts for *cis*-AB within irradiated **1**⊃$AB_{1.0}$ at 242 K compared to the static model (blue) and rotation averaged model (grey).

**S30.** Data for the endothermic transition (1) of **1**⊃$AB_x$. First heating branch. 0 – 200 ˚C at 20 ˚C $min^{-1}$.

| | Energy / J $g^{-1}$ | onset / ˚C | Beginning of transition / ˚C | End of transition / ˚C | Range / ˚C |
|---|---|---|---|---|---|
| **1**⊃$AB_{1.0}$ | 2.2 | 156.4 | 150 | 170 | 20 |
| **1**⊃$AB_{0.9}$ | 2.9 | 155.1 | 149 | 168 | 19 |
| **1**⊃$AB_{0.5}$ | 1.3 | 148.1 | 144 | 164 | 20 |
| **1**⊃$AB_{0.3}$ | 2.1 | 116.5 | 113 | 134 | 21 |

**S31.** Data for the exothermic transition (1) of **1**⊃$AB_x$. First cooling branch. 0 – 200 ˚C at 20 ˚C $min^{-1}$.

| | energy / J $g^{-1}$ | onset / ˚C | Begin of transition / ˚C | End of transition / ˚C | Range / ˚C |
|---|---|---|---|---|---|
| **1**⊃$AB_{1.0}$ | 27.9 | 159.2 | 125 | 175 | 50 |
| **1**⊃$AB_{0.9}$ | 25.0 | 162.9 | 145 | 170 | 25 |
| **1**⊃$AB_{0.5}$ | 12.8 | 158.9 | 140 | 170 | 30 |
| **1**⊃$AB_{0.3}$ | 5.0 | 125.2 | 105 | 130 | 25 |

**S32.** Data for the exothermic transition (2) of **1**⊃$AB_x$. First heating branch. 0 – 200 ˚C at 20 ˚C $min^{-1}$.

| | energy / J $g^{-1}$ | onset/ ˚C | Beginning of transition / ˚C | End of transition /˚C | Range / ˚C |
|---|---|---|---|---|---|
| **1**⊃$AB_{1.0}$ | 2.4 | 180.7 | 178 | 195 | 17 |
| **1**⊃$AB_{0.9}$ | 1.5 | 171.7 | 170 | 179 | 9 |
| **1**⊃$AB_{0.5}$ | 1.2 | 171.4 | 170 | 181 | 11 |
| **1**⊃$AB_{0.3}$ | n/a | n/a | n/a | n/a | n/a |

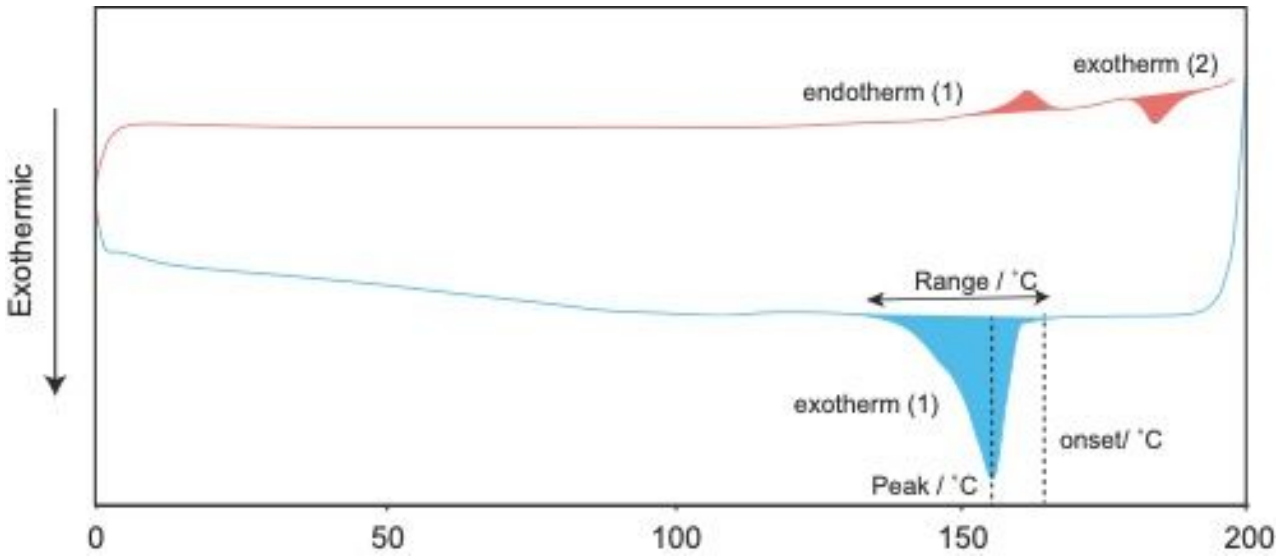

Key - DSC cycle for **S29** – **S31**. First heating branch (orange). First cooling branch (blue).

**S33**. DSC data for **1**⊃$AB_x$ after irradiation over the first heating/cooling cycle. 0 – 200 ˚C at 20 ˚C $min^{-1}$.

| Compound | cis %[a] | Endotherm(1) / kJ $mol^{-1}$ | Exotherm(2) / kJ $mol^{-1}$ | Exotherm (1) / kJ $mol^{-1}$ |
|---|---|---|---|---|
| **1**⊃$AB_{1.0}$ | 40 | 1.6 | 1.8 | 21.2 |
| **1**⊃$AB_{0.9}$ | 38 | 2.1 | 1.1 | 18.5 |
| **1**⊃$AB_{0.5}$ | 31 | 0.9 | 0.8 | 8.6 |
| **1**⊃$AB_{0.3}$ | 13 | 1.3 | 0 | 3.2 |

(a) Calculated by solvent extraction (MeOH-$_{d4}$) and $^1$H NMR spectroscopy.

**S34.** Graph to show the decrease in endothermic (1) transition enthalpy of **1**⊃$AB_{1.0}$ with the increasing proportion of *cis*-AB.

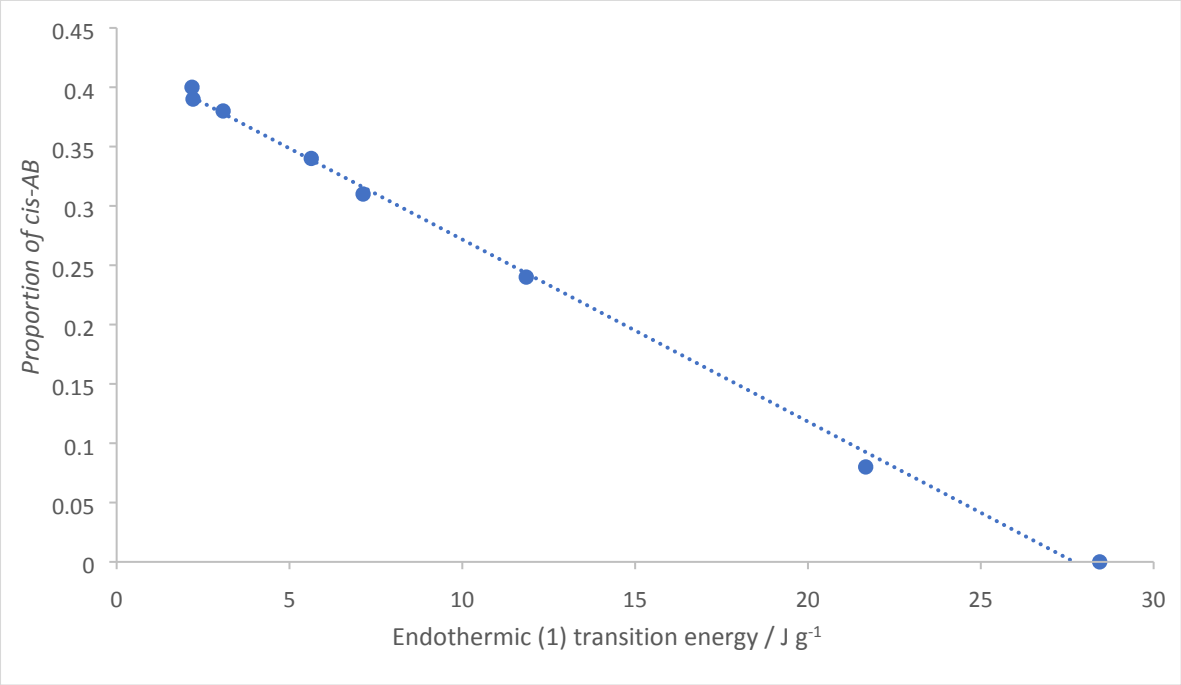

**S35.** Calculated energy difference between *trans*-AB and *cis*-AB.

| | (energy/molecule) / (eV/molecule) | (energy/mole) / eV $mol^{-1}$ | (energy/mole) / J $mol^{-1}$ | (energy/g) / J $g^{-1}$ |
|---|---|---|---|---|
| *trans*-AB | -2603.707821 | $-1.5679895255 \times 10^{27}$ | $-2.512201458 \times 10^{8}$ | $-1.3786185605 \times 10^{6}$ |
| *cis*-AB | -2603.164885 | $-1.5676625620 \times 10^{27}$ | $-2.5116776036 \times 10^{8}$ | $-1.3783310854 \times 10^{6}$ |
| Energy difference | -0.542935646 | $-3.2696349381 \times 10^{23}$ | $-5.2385437052 \times 10^{4}$ | $-2.8747509714 \times 10^{2}$ |

- The energy difference between isolated *cis* and *trans*-AB per gram is -288.48 J $g^{-1}$.
- The photo-stationary state between *cis* and *trans*-AB *cis:trans* within **1**⊃$AB_{1.0}$ is 0.40.
- -288.48 J $g^{-1}$ x 0.40 = -114.9 J $g^{-1}$

The mass of **1** must be accounted for as well as the proportion of *trans*-azobenzene within **1**⊃$AB_{1.0}$.

- **1**⊃$AB_{1.0}$ = $[Zn_2(BDC)_2(DABCO)(AB)]$

| | RMM (g/mol) | Fractional mass of AB | (energy/gram)/ (J $g^{-1}$) |
|---|---|---|---|
| **1** | 579.3 | 1.00 | n/a |
| **1**⊃$AB_{1.0}$ | 761.4 | 0.24 | 26.1 |
| **1**⊃$AB_{0.9}$ | 739.6 | 0.22 | 23.7 |
| **1**⊃$AB_{0.5}$ | 674.0 | 0.14 | 15.4 |
| **1**⊃$AB_{0.3}$ | 639.0 | 0.09 | 10.3 |

**S36.** Observed energy difference on the first heating branch between **1**⊃$AB_x$ and UV irradiated **1**⊃$AB_x$.

| Compound | Endotherm (1) / J $g^{-1}$ | *cis-trans* exotherm (2) / J $g^{-1}$ | Exotherm (1) / J $g^{-1}$ | Energy difference on heating branch / J $g^{-1}$ |
|---|---|---|---|---|
| **1**⊃$AB_{1.0}$ | 2.2 | 2.4 | 27.9 | -28.1 |
| **1**⊃$AB_{0.9}$ | 2.9 | 1.5 | 25.0 | -24.1 |
| **1**⊃$AB_{0.5}$ | 1.3 | 1.2 | 12.8 | -12.7 |
| **1**⊃$AB_{0.3}$ | 2.1 | 0.00 | 5.0 | -2.9 |

**S37.** Difference between observed energy difference on the first heating branch for UV irradiated **1**⊃$AB_x$ and calculated *cis-trans* AB thermal relaxation energies.

| Time / min | Energy difference on heating Branch / J $g^{-1}$ | cis photo / % | Correction for PSS / J $g^{-1}$ | Calculated energy difference / J $g^{-1}$ | Difference between calc and obs / J $g^{-1}$ |
|---|---|---|---|---|---|
| **1**⊃$AB_{1.0}$ | -28.1 | 0.40 | -114.9 | -27.5 | -0.6 |
| **1**⊃$AB_{0.9}$ | -24.1 | 0.38 | -109.2 | -23.7 | -0.4 |
| **1**⊃$AB_{0.5}$ | -12.7 | 0.31 | -89.1 | -12.5 | -0.2 |
| **1**⊃$AB_{0.3}$ | -2.9 | 0.13 | -37.4 | -3.5 | 0.6 |

**S38.** Observed energy difference on the first heating branch between pre-irradiated **1**⊃$AB_{1.0}$ and UV irradiated **1**⊃$AB_{1.0}$.

| Time / min | Endothermic transition (1) / J $g^{-1}$ | *cis-trans* exotherm (2) / J $g^{-1}$ | exothermic transition (1) / J $g^{-1}$ | Energy difference on heating Branch / J $g^{-1}$ |
|---|---|---|---|---|
| 0 | 28.4 | 0 | 28.0 | 0.5 |
| 30 | 21.7 | 0 | 27.8 | -6.1 |
| 60 | 11.9 | 1.5 | 27.6 | -17.2 |
| 90 | 7.1 | 1.8 | 27.8 | -22.4 |
| 120 | 5.6 | 2.0 | 27.3 | -23.7 |
| 180 | 3.1 | 2.3 | 28.0 | -27.2 |
| 240 | 2.2 | 2.4 | 27.9 | -28.1 |
| 300 | 2.2 | 2.4 | 28.0 | -28.2 |

**S39.** Difference between observed energy difference on the first heating branch for irradiated **1**⊃$AB_{1.0}$ and calculated *cis-trans* AB thermal relaxation energies.

| Time / min | cis photo / % | Correction for PSS / J $g^{-1}$ | Calculated energy difference / J $g^{-1}$ | Difference between calc and obs / \ J $g^{-1}$ |
|---|---|---|---|---|
| 0 | 0.00 | 0 | 0 | -0.5 |
| 30 | 0.08 | -23.0 | -5.5 | -0.6 |
| 60 | 0.24 | -69.0 | -16.5 | -0.7 |
| 90 | 0.31 | -89.1 | -21.3 | -1.1 |
| 120 | 0.34 | -97.7 | -23.4 | -0.3 |
| 180 | 0.38 | -109.2 | -26.1 | -1.1 |
| 240 | 0.39 | -112.1 | -26.8 | -1.2 |
| 300 | 0.40 | -115.0 | -27.5 | -0.7 |

**S40.** Data from endothermic (1) transition of **1**⊃$AB_{1.0}$ with UV irradiation time. First heating branch. 0 – 200 ˚C at 20 ˚C $min^{-1}$.

| Time/ minutes | energy / J $g^{-1}$ | onset/ ˚C | peak/ ˚C | Beginning of transition / ˚C | End of transition / ˚C | Range / ˚C |
|---|---|---|---|---|---|---|
| 0 | 28.4 | 161.6 | 165.7 | 150.0 | 180.0 | 30.0 |
| 30 | 21.7 | 158.9 | 164.5 | 150.0 | 176.0 | 26.0 |
| 60 | 11.9 | 157.4 | 162.2 | 150.0 | 173.0 | 23.0 |
| 90 | 7.1 | 157.0 | 165.8 | 150.0 | 173.0 | 23.0 |
| 120 | 5.6 | 156.9 | 163.4 | 150.0 | 172.0 | 22.0 |
| 180 | 3.1 | 156.6 | 162.8 | 150.0 | 171.0 | 21.0 |
| 240 | 2.2 | 156.4 | 162.0 | 150.0 | 170.0 | 20.0 |
| 300 | 2.2 | 156.1 | 162.0 | 150.0 | 171.0 | 21.0 |

**S41.** Data from exothermic transition (1) of **1**⊃$AB_{1.0}$ with UV irradiation time. First cooling branch. 0 – 200 ˚C at 20 ˚C $min^{-1}$.

| | energy / J $g^{-1}$ | onset/ ˚C | peak/ ˚C | Beginning of transition / ˚C | End of transition / ˚C | Range / ˚C |
|---|---|---|---|---|---|---|
| 0 | 28.0 | 160.9 | 157.4 | 175 | 125 | 50 |
| 30 | 28.8 | 160.6 | 157.1 | 175 | 125 | 50 |
| 60 | 27.6 | 158.7 | 154.9 | 175 | 125 | 50 |
| 90 | 27.8 | 161.7 | 160.4 | 175 | 125 | 50 |
| 120 | 27.3 | 161.1 | 157.8 | 175 | 125 | 50 |
| 180 | 28.0 | 160.0 | 157.0 | 175 | 125 | 50 |
| 240 | 27.9 | 159.5 | 156.1 | 175 | 125 | 50 |
| 300 | 28.0 | 159.6 | 156.8 | 175 | 125 | 50 |

**S42.** Data from exothermic transition (2) from **1**⊃$AB_{1.0}$ with UV irradiation time. First heating branch. 0 – 200 ˚C at 20 ˚C $min^{-1}$.

| Time /minutes | energy / J $g^{-1}$ | onset / ˚C | peak/ ˚C | Beginning of transition / ˚C | End of transition / ˚C | Range / ˚C |
|---|---|---|---|---|---|---|
| 60 | 1.5 | 176.4 | 183.0 | 176 | 190 | 14 |
| 90 | 1.8 | 179.2 | 183.2 | 177 | 192 | 15 |
| 120 | 2.0 | 179.9 | 183.5 | 178 | 194 | 16 |
| 180 | 2.3 | 180.6 | 183.9 | 178 | 195 | 17 |
| 240 | 2.4 | 180.7 | 183.9 | 178 | 195 | 17 |
| 300 | 2.4 | 180.7 | 183.9 | 178 | 195 | 17 |

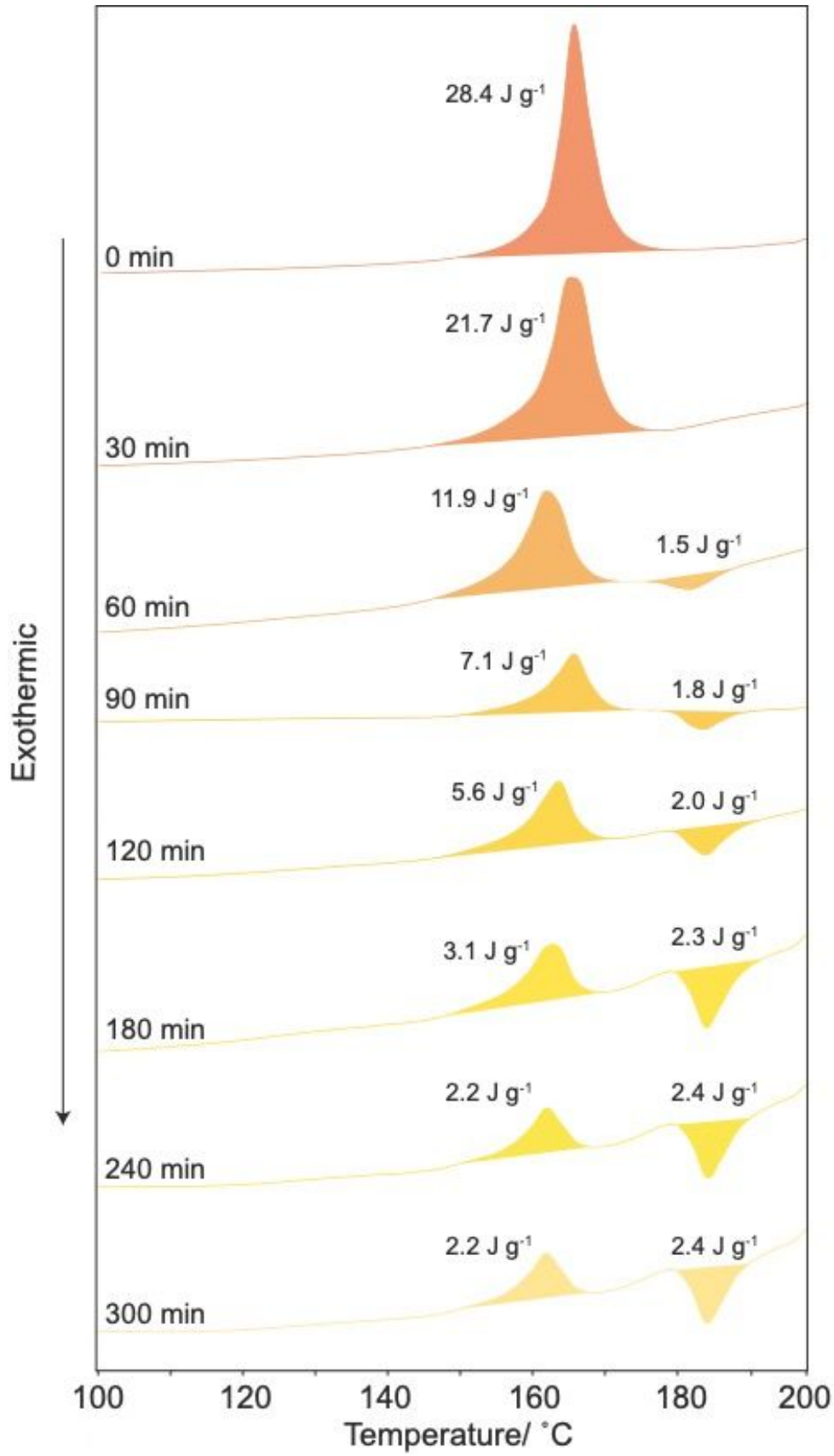


**S43.** DSC cycles of **1**⊃$AB_{1.0}$ at different irradiation times between 100 – 200 ˚C at a rate of 20 ˚C $min^{-1}$.

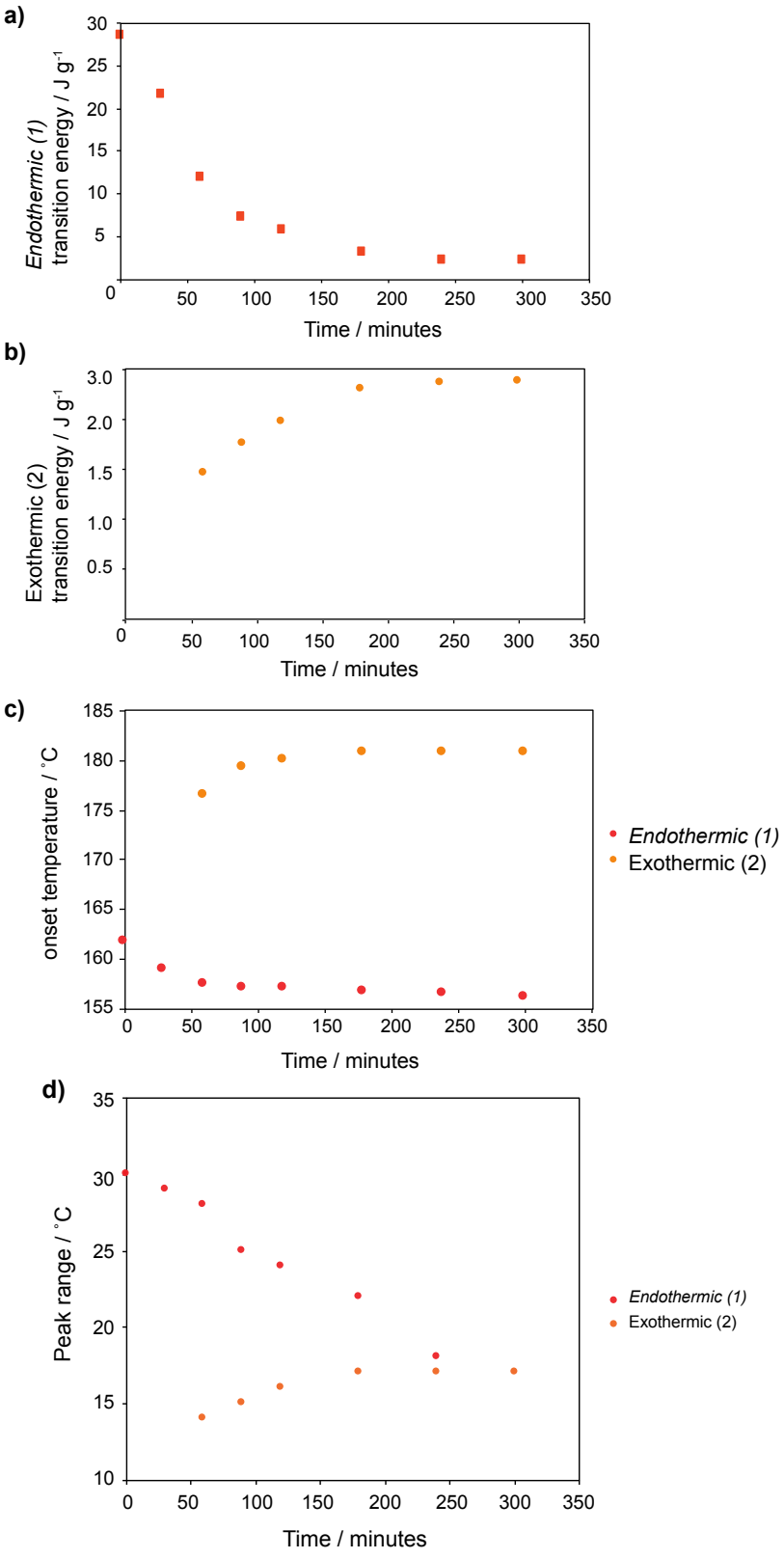


**S44.** Relationships between irradiation time and thermal properties of **1**⊃$AB_{1.0}$. a) Dependence of endothermic (1) enthalpy on UV irradiation time. b) The increase of exothermic (2) transition energy with irradiation time. c) Variation of endothermic (1) transition and exothermic (2) transition onset temperatures with irradiation. d) Convergence of temperature range for both endothermic (1) and exothermic (2) transitions.

**S45.** Onset temperature and energies for the endothermic (1) transition and exothermic(2) transition on the first heating branch for irradiated **1**⊃$AB_{1.0}$ at different heating rates.

| Heating Rate/ ˚C $min^{-1}$ | Endothermic (1) / J $g^{-1}$ | Endothermic (1) onset / ˚C | Exothermic (2) / J $g^{-1}$ | Exothermic (2) onset / ˚C |
|---|---|---|---|---|
| 5 | 2.4 | 152.8 | 2.3 | 164.2 |
| 10 | 2.3 | 152.7 | 2.2 | 171.1 |
| 15 | 2.2 | 152.6 | 2.4 | 175.0 |
| 20 | 2.3 | 152.0 | 2.4 | 178.2 |

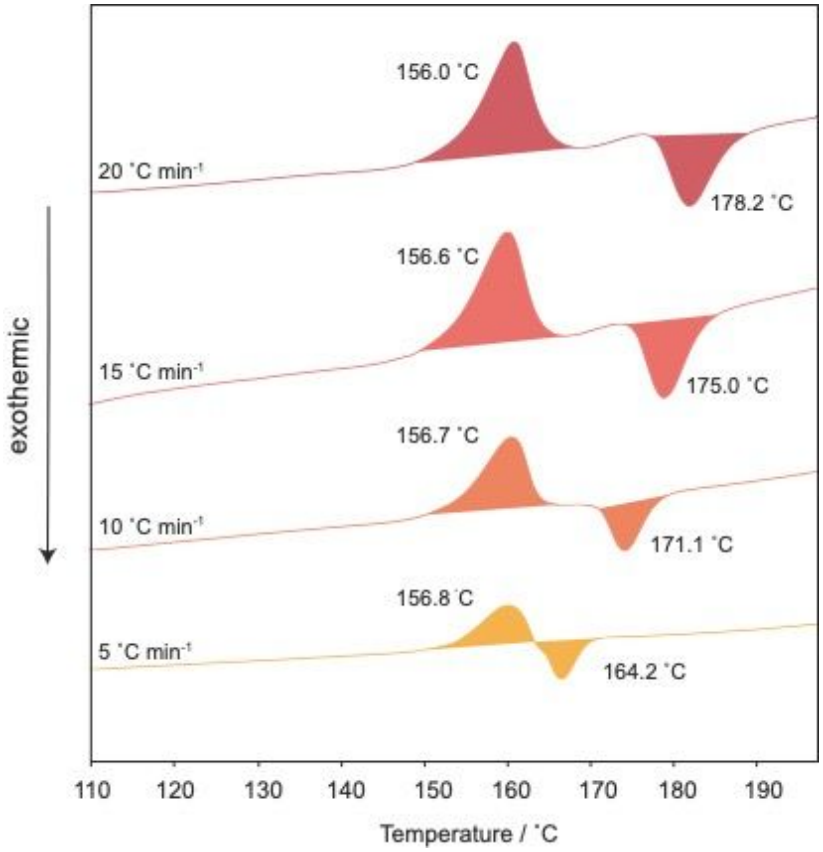


**S46.** DSC trace of **1**⊃$AB_{1.0}$ irradiated with 365 nm light for 300 minutes between 0 – 200 ˚C at different heating rates. First heating branch (red).

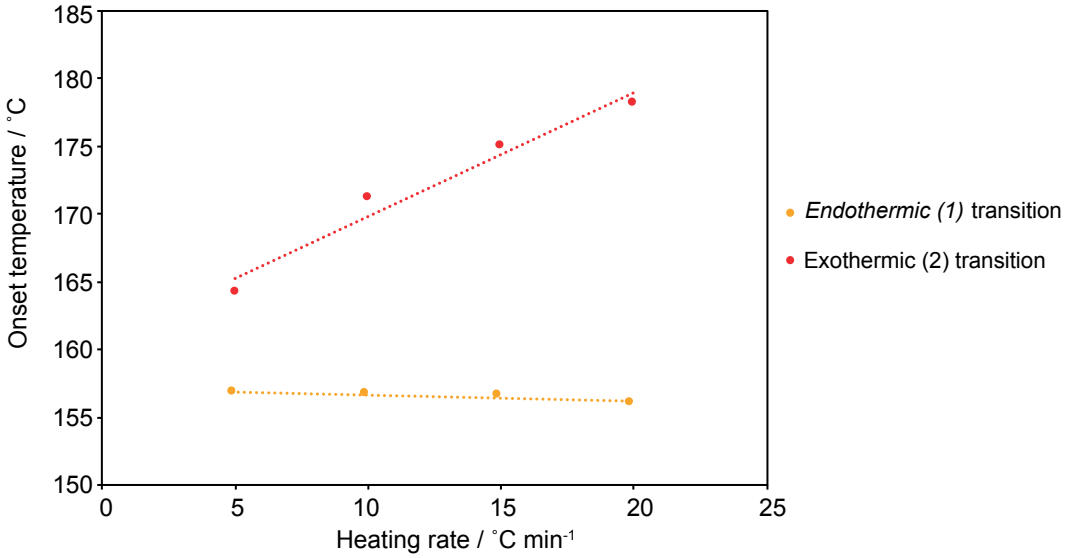


**S47.** Relationship between the onset temperature of the endothermic (1) and the exothermic (2) transition on the first heating branch.

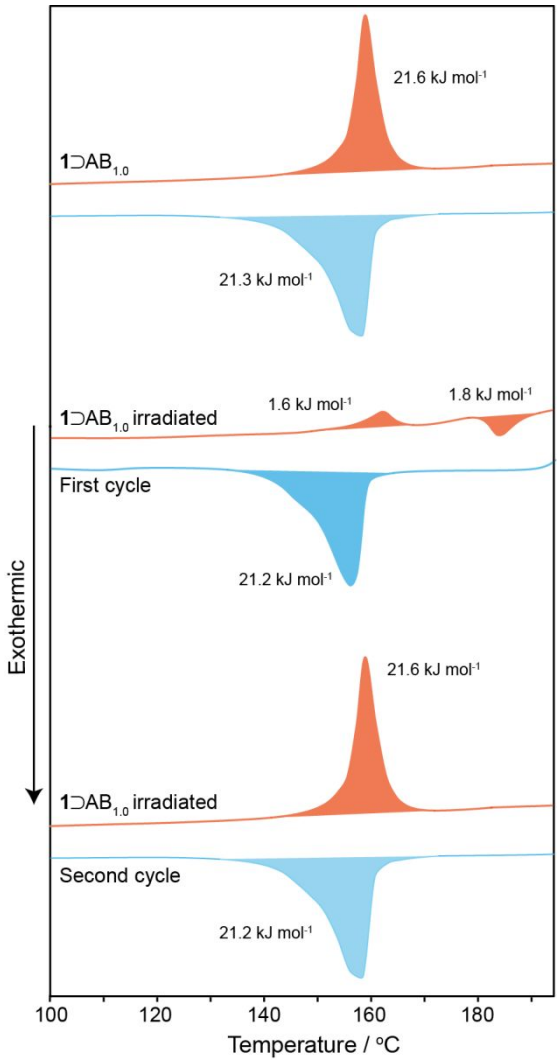


**S48.** DSC cycles showing the effect of irradiation and heat treatment on **1**⊃$AB_{1.0}$ at 20 ˚C $min^{-1}$.

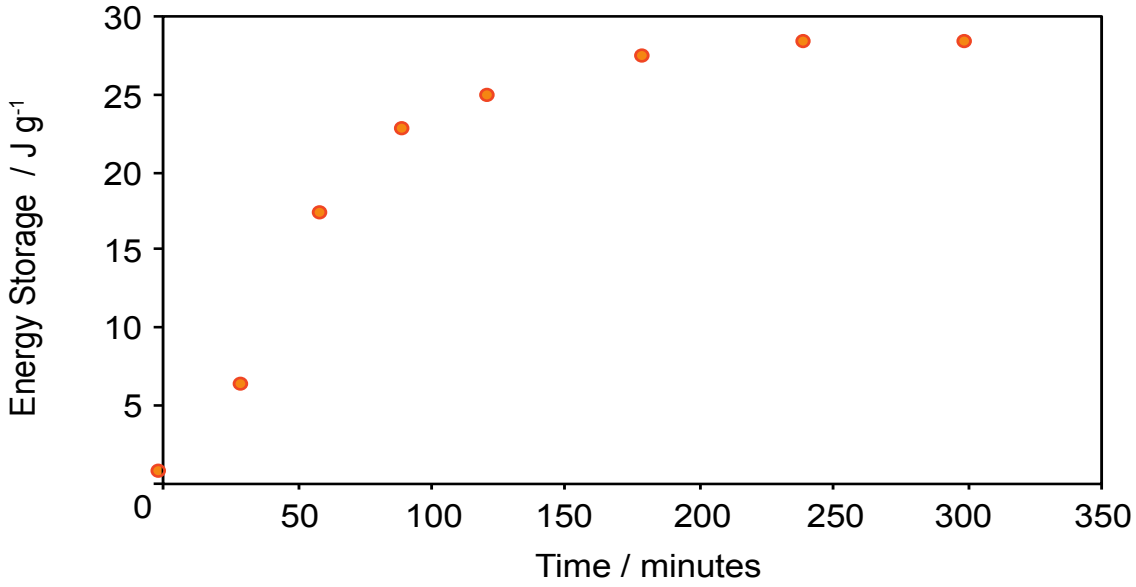


**S49.** Net energy storage of **1**⊃$AB_{1.0}$ at different irradiation times.

**S50.** Half-life calculation.

| Time / months | proportion *cis*-AB | $N_{(t)}/N_{(0)}$ | $Ln(N_{(t)}/N_{(0)})$ |
|---|---|---|---|
| 0 | 0.4 | 1 | 0 |
| 1 | 0.39 | 0.975 | -0.025317808 |
| 2 | 0.39 | 0.975 | -0.025317808 |
| 3 | 0.38 | 0.95 | -0.051293294 |
| 4 | 0.38 | 0.95 | -0.051293294 |

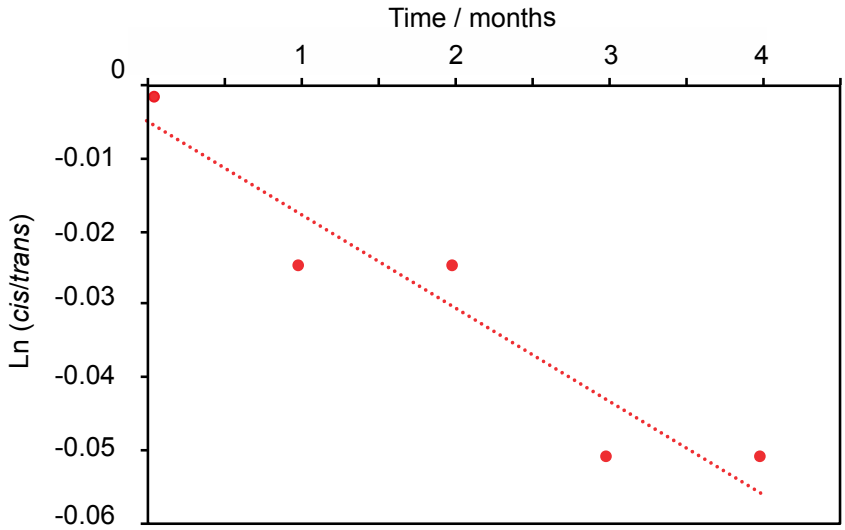


Assuming the metastable *cis* isomer undergoes thermal reconversion to the ground-state *trans* isomer according to first-order kinetics, the number of guest molecules in the *cis* isomeric state as a function of time ($N_{cis}(t)$) can be expressed by

$$N_{cis}(t) = N_{cis}(0)e^{-\lambda t}$$

where $N_{cis}(0)$ is the number of guest molecules in the *cis* isomeric state at the beginning of the measurement and $\lambda$ is a decay constant. This rearranges to the following form whereby plotting $\ln(N_{cis}(t)/N_{cis}(0))$ vs $t$ allows determination of $\lambda$ from the gradient of the straight line of best fit.

$$ln\left(\frac{N_{cis}(t)}{N_{cis}(0)}\right) = -\lambda t$$

The half-life, $t_{½}$ , then given by

$$t_{\frac{1}{2}} = \frac{ln2}{\lambda}$$

For **1**⊃$AB_{1.0}$ a decay constant, $\lambda$, of 0.0129 month$^{-1}$ was determined, corresponding to a half-life of 53.7 months, or ~4.5 years for the *cis* isomer.

## References


(1) Segall, M. D.; Lindan, P. J. D.; Probert, M. J.; Pickard, C. J.; Hasnip, P. J.; Clark, S. J.; Payne, M. C. First-Principles Simulation: Ideas, Illustrations and the CASTEP Code. *J. Phys. Condens. Matter* **2002**, *14* (11), 2717–2744. https://doi.org/10.1088/0953-8984/14/11/301.

(2) Pickard, C. J.; Mauri, F. All-Electron Magnetic Response with Pseudopotentials: NMR Chemical Shifts. *Phys. Rev. B* **2001**, *63* (24), 245101. https://doi.org/10.1103/PhysRevB.63.245101.

(3) Perdew, J. P.; Burke, K.; Ernzerhof, M. Generalized Gradient Approximation Made Simple. *Phys. Rev. Lett.* **1996**, *77* (18), 3865–3868. https://doi.org/10.1103/PhysRevLett.77.3865.

(4) Yates, J. R.; Pickard, C. J.; Mauri, F. Calculation of NMR Chemical Shifts for Extended Systems Using Ultrasoft Pseudopotentials. *Phys. Rev. B* **2007**, *76* (2), 24401. https://doi.org/10.1103/PhysRevB.76.024401.

(5) Grimme, S. Semiempirical GGA-Type Density Functional Constructed with a Long-Range Dispersion Correction. *J. Comput. Chem.* **2006**, *27* (15), 1787–1799. https://doi.org/10.1002/jcc.20495.

(6) Dybtsev, D. N.; Chun, H.; Kim, K. Rigid and Flexible: A Highly Porous Metal-Organic Framework with Unusual Guest-Dependent Dynamic Behavior. *Angew. Chemie - Int. Ed.* **2004**, *43* (38), 5033–5036. https://doi.org/10.1002/anie.200460712.

(7) Wilson, C. C.; Myles, D.; Ghosh, M.; Johnson, L. N.; Wang, W. Neutron Diffraction Investigations of L- and d-Alanine at Different Temperatures: The Search for Structural Evidence for Parity Violation. *New J. Chem.* **2005**, *29* (10), 1318–1322. https://doi.org/10.1039/B419295H.